JGS
Journal of the Geological Society

Research article

https://doi.org/10.1144/jgs2020-215 | Vol. 178 | 2021 | jgs2020-215

Tracking Proterozoic–Triassic sediment routing to western Laurentia via bivariate non-negative matrix factorization of detrital provenance data

Joel E. Saylor[1]* and Kurt E. Sundell[2]

[1] Department of Earth, Ocean and Atmospheric Sciences, University of British Columbia, Vancouver, BC, Canada
[2] Department of Geosciences, University of Arizona, Tucson, AZ, USA
JES, 0000-0001-7746-862X; KES, 0000-0002-5290-4285
*jsaylor@eoas.ubc.ca

Abstract: When reconstructing sediment provenance, the challenge posed by multiple univariate (i.e., age-only) detrital geochronology data sets with similar one-dimensional distributions can be mitigated by incorporation of a second variable such as Hf isotopic data. However, there is no commonly applied method of sample intercomparison, much less forward or inverse modeling of these bivariate data sets. In this paper we explore application of non-negative matrix factorization (NMF) to bivariate data sets. Factorization of univariate mixed (a.k.a., sink or daughter) data sets has been demonstrated to successfully recover both the one-dimensional endmember (a.k.a., source or parent) distributions and their mixture weightings. We show that NMF can successfully recover both the two-dimensional distributions and mixing weights in synthetic data sets. Application of the method to 24 published Neoproterozoic–Triassic samples from western Laurentia yields six two-dimensional endmember distributions that are a close match to empirical sediment sources on the southern, eastern, and northern margin of Laurentia. The results are broadly consistent with previous interpretations and confirm that the method can characterize unknown sediment sources based on data from analyzed sink samples. Correlating between factorized endmembers and empirical sources indicates that the Transcontinental Arch was not a barrier to east–west sediment transport until the late Cambrian. Quantitative comparison also shows that the closest known match for a factorized endmember with highly evolved Permo-Triassic zircons is from northern South America and suggests northward transport of this detritus following assembly of Pangea. Recognizing these empirical sources and their distribution into strata that would later be incorporated into the North American Cordillera sets the stage for interpreting sediment provenance records in the Jurassic–Paleogene Cordilleran retroarc foreland basin.

Supplementary material: The open-source software (*DZnmf2D*) and a user manual is available in public repositories: https://doi.org/10.5281/zenodo.4460336. All other supplemental files are available at https://doi.org/10.6084/m9.figshare.c.5280320

Thematic collection: This article is part of the Fold-and-thrust belts and associated basins collection available at: https://www.lyellcollection.org/cc/fold-and-thrust-belts

Received 13 November 2020; **revised** 19 January 2021; **accepted** 21 January 2021

Although detrital geochronology has become a standard part of the tectonic, sedimentary, and basin analysis toolbox, uncertainties introduced by non-unique age distributions continue to hamper robust interpretations. Similar age distributions may result from recycling (e.g. Dickinson *et al.* 2009), or synchronous magmatism or metamorphism across a wide geographic area (e.g. Smith *et al.* 2019). Whatever the cause, similar age distributions hamper both quantitative and qualitative comparison methods (e.g. Thomas 2011). The challenge presented by similar univariate age distributions is exemplified in the complex sediment routing system in the late Paleozoic in Laurentia.

Laurentia has multiple regions with similar magmatic histories which yield similar zircon U–Pb age distributions. For example, multiple regions along the margin of Laurentia or in peri-Gondwanan terranes experienced late Neoproterozoic–early Paleozoic magmatism or metamorphism, yielding overlapping zircon U–Pb ages. Similarly, the Mojave crustal block and Yavapai–Mazatzal terrane have *c.* 1.6–2.0 Ga zircon U–Pb ages that overlap with regions of the northeastern Canadian shield (Bickford *et al.* 2008; Røhr *et al.* 2008, 2010; Wooden *et al.* 2013). As a final example, Permo–Triassic magmatism occurred along both the western margin of Laurentia and northern South America. Permo–Triassic zircons from Triassic strata in Sonora, Utah, and Nevada may have sources to the north which also shed sediment to the Sverdup Basin (Røhr *et al.* 2010; Midwinter *et al.* 2016), from local Permo–Triassic plutons (Cecil *et al.* 2019), or basement of northwestern Gondwana (Cochrane 2013). These similar age distributions have confounded interpretive approaches that rely on the presence or absence of age modes in specific age ranges. These limitations are partly addressed using statistical measures of similarity between sink and source samples (e.g. Leary *et al.* 2020). Nevertheless, uncertainty persists even with statistical comparison, as indicated by variable attribution of late Neoproterozoic–early Paleozoic zircons to peri-Gondwana terranes accreted to eastern Laurentia or those from South or Central America (Gleason *et al.* 2007; Kissock *et al.* 2018; Liu and Stockli 2019).

The inability to resolve sediment sources using one-dimensional (age) distributions necessitates an alternative approach. This has been successfully addressed with multivariate approaches (e.g. Gehrels and Pecha 2014; Linde *et al.* 2016, 2017; Thomas *et al.* 2020; Waite *et al.* 2020). Distinct sources may have unique thermal histories, Hf isotopic compositions at the time of zircon crystallization (εHf_T), oxygen isotope compositions, rare-earth element concentrations, or Th/U ratios (e.g. Belousova *et al.* 2002; Hoskin and Schaltegger 2003; Rahl *et al.* 2003; Fu *et al.* 2008;

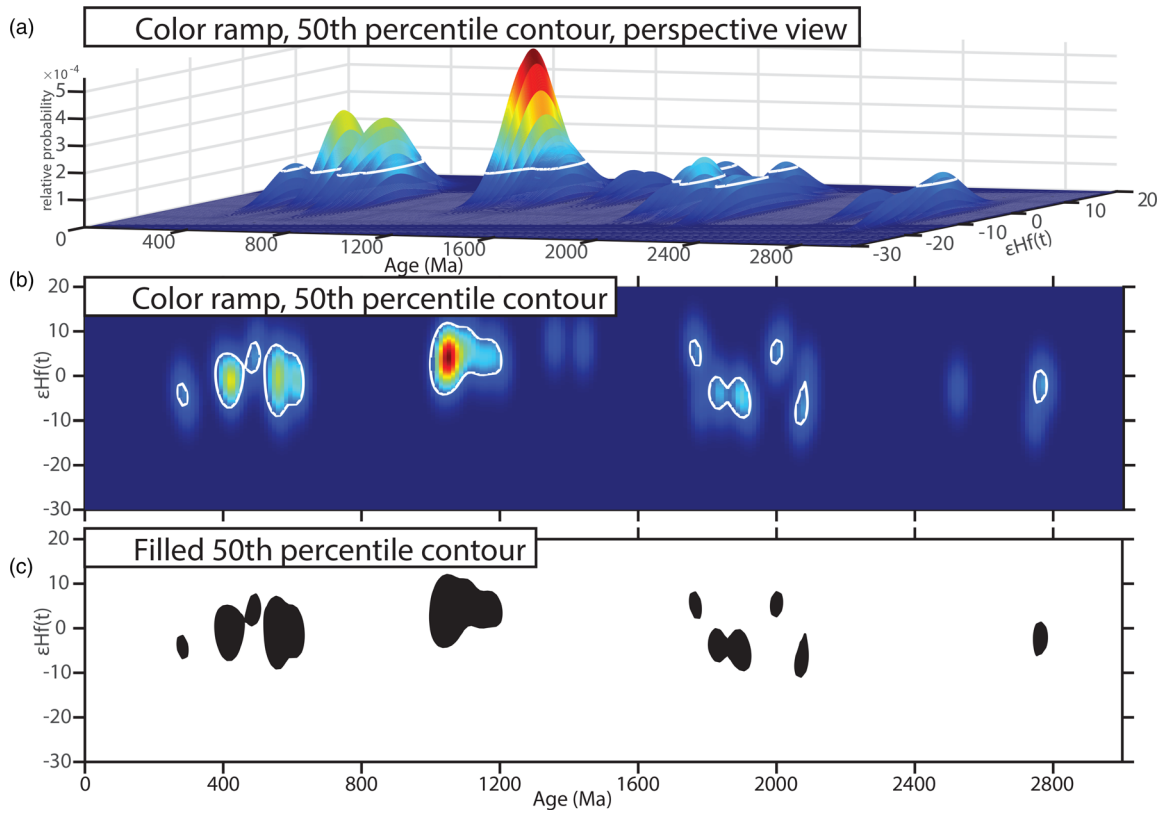

Fig. 1. Bivariate data sets are considered as two-dimensional kernel density estimates (KDEs). These can be visualized as (**a**) three-dimensional volumes, (**b**) two-dimensional intensity maps, with or without contours, or (**c**) clipped contour plots. In all three cases, the underlying data are identical and so comparison metrics or non-negative matrix factorization of these data sets will be the same. In this case, KDEs are based on a 20 Myr bandwidth for age, and a 4 ε-unit bandwidth for εHf_T.

Mueller *et al.* 2008; Flowerdew *et al.* 2009; Appleby *et al.* 2010; Cecil *et al.* 2011; Anfinson *et al.* 2012). Bivariate petrochronological approaches use this secondary variable in addition to grain ages to refine attribution of detrital grains or groups of grains to specific sources (e.g. Gehrels and Pecha 2014). For example, in the case of the late Paleozoic samples discussed above, systematic variations in the Hf isotopic compositions of zircons have been used to discriminate between sources in the Franklinian Basin, which have positive ('juvenile') εHf_T values, and sources along the Iapetus suture in eastern Laurentia, which have more negative ('evolved') εHf_T values.

Qualitative interpretations of bivariate data sets limit both the objectivity of those interpretations and also the ability to model the two-dimensional distributions (Sundell and Saylor 2021). For example, cross-plots of zircon U–Pb ages and εHf_T values are often compared to fields representing source areas in order to assess the overlap between samples and sources (e.g. Gehrels and Pecha 2014 and many others). Although providing insight and potentially discriminatory power, this approach does not leverage the modal proportions of age/εHf_T distributions to determine whether multiple sources may have contributed to a particular sample. Comparison of measured age/εHf_T pairs to source fields also provides no basis for forward or inverse modeling of sediment mixing.

In this paper we develop a non-negative matrix factorization (NMF) approach to reconstructing unknown two-dimensional endmember (a.k.a. source or parent) distributions based on known two-dimensional distributions from mixed (a.k.a. sink or daughter) samples. We first demonstrate that the algorithm is able to reconstruct both the age and εHf_T distributions, and the mixing weights based on factorization of sinks randomly mixed from known endmembers. We next apply the algorithm to a suite of 24 Neoproterozoic–Triassic samples from central–western Laurentia. The algorithm identifies endmembers that match empirical sediment sources and suggests sediment transport pathways that are largely consistent with previous interpretations. It also refines identification of the source of Paleoproterozoic and Permo-Triassic zircons.

Methods

Non-negative matrix factorization

Here we extend the NMF approach, which Sharman and Johnstone (2017) and Saylor *et al.* (2019) applied to univariate data sets and one-dimensional distributions, to bivariate data sets and two-dimensional distributions. The difference between these approaches is similar to that between signal processing applications of NMF to waveforms (e.g. Raj *et al.* 2010) and image processing applications of NMF to hyperspectral images (e.g. Rajabi and Ghassemian 2014). In both instances, given a matrix V (composed of m features from n samples) NMF seeks to develop two matrices W (m-by-k) and H (k-by-n) such that

$$V = WH + E \tag{1}$$

where E is the final residual. In the NMF algorithm implemented here E is calculated as the Frobenius norm of V–WH and is calculated as

$$E = \sqrt{\sum_{i=1}^{m}\sum_{j=1}^{n} |V_{ij} - (WH)_{ij}|^2}. \tag{2}$$

Data are input to the algorithm as two-dimensional kernel density estimates (KDEs) with fixed bandwidths (Fig. 1) (Andersen 2014; Roberts and Spencer 2015; Spencer *et al.* 2019). Discrete data

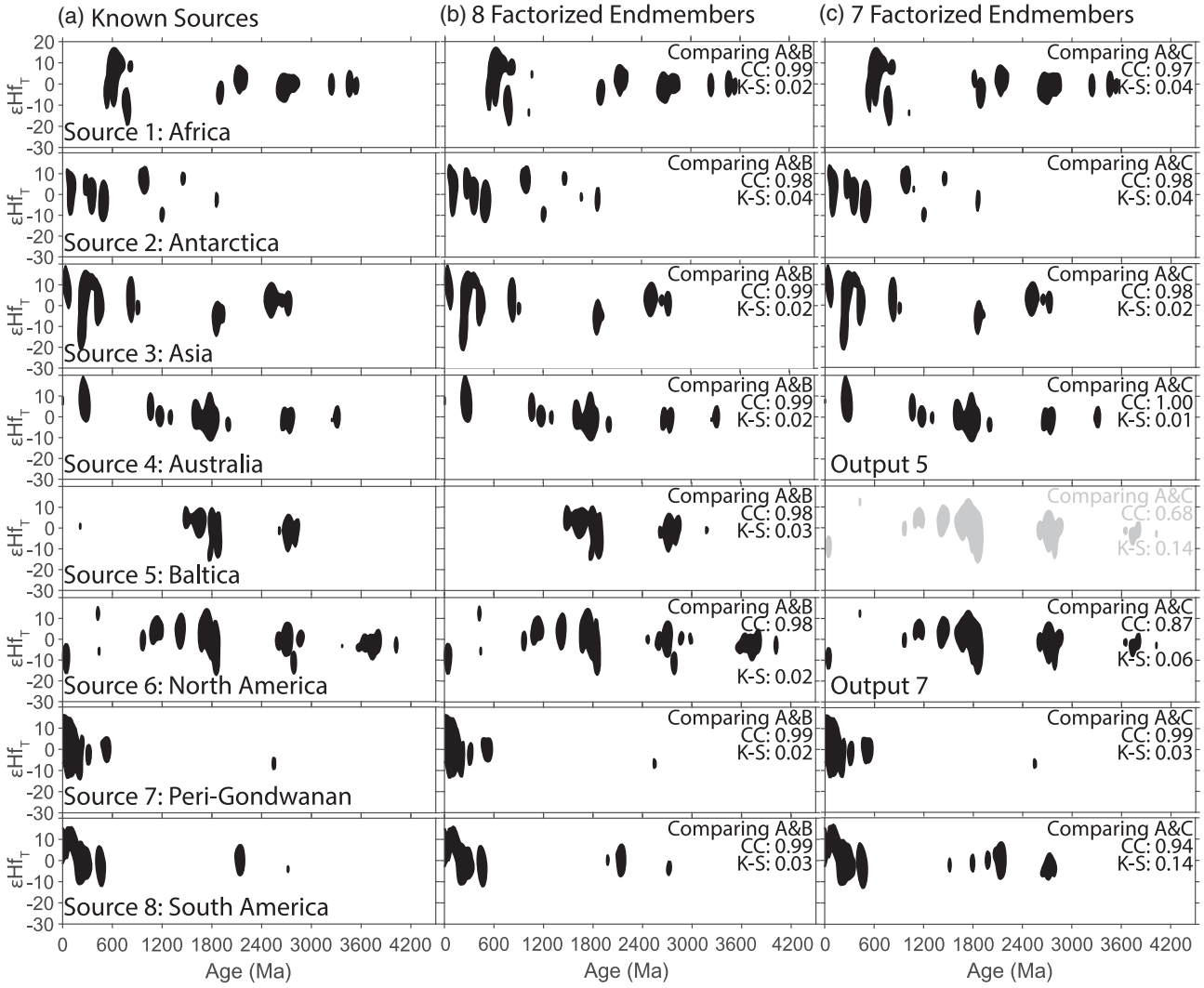

Fig. 2. Comparison of known sources and factorized endmembers for the eight-source data set. (**a**) Eight source kernel density estimates that were used as sources and mixed to form 40 random sink samples. (**b**) Factorization of the 40 samples to eight endmembers yields distributions that closely match the original five sources as indicated by cross-correlation values approaching 1 and D values approaching 0. (**c**) Factorization of the 40 sink samples to seven endmembers yields distribution that match the original five more poorly. KDEs are based on a 20 Myr bandwidth for age, and a 4 ε-unit bandwidth for εHf_T and are plotted as the contour of the median (50th percentile). Abbreviations: CC: cross-correlation coefficient, K-S: Kolmogorov–Smirnov D-value.

points (i.e. age and εHf_T) are transformed to two-dimensional distributions following the approach outlined by Sundell *et al.* (2019) and Sundell and Saylor (2021). Briefly, the transformation proceeds by first performing a discrete cosine transform of each discrete data set (Ahmed *et al.* 1974). The resulting two-dimensional matrix of points is multiplied by a Gaussian function based on the defined kernel bandwidths. The resulting matrix is then inverted using the discrete cosine transform. Finally, the matrix is normalized so that the resulting three-dimensional volume integrates to 1. The result is a two-dimensional matrix of *z*-axis values that can be visualized as a three-dimensional volume where the density is displayed as height in the *z*-axis direction (Fig. 1a) or as a two-dimensional plot of clustering of ages and εHf_T ('density', color-coded as intensity (Fig. 1b). For all analyses presented here the bandwidth for age is 20 Myr and that for εHf values is four εHf units.

Rank estimation

We tested two methods to identify the optimum rank for factorization. These are the segmented linear regression breakpoint-analysis used by Saylor *et al.* (2019) and a bi-cross-validation method developed by Owen and Perry (2009). We also considered Akaike's information criterion (Akaike 1974), Bayesian information criterion (Schwarz 1978), and minimum length description (Squires *et al.* 2017). However, we rejected all of these because in the analysis of Fu *et al.* (2019) bi-cross-validation more accurately estimated the true rank at low ranks (i.e. ranks <25) than any of the alternatives, and we anticipate that factorization of detrital data sets should yield fewer than 25 potential sources. As an example of the expected number of endmembers, Laskowski *et al.* (2013) grouped samples spanning the North American Cordilleran retroarc into seven characteristic groups based on their detrital zircon U–Pb age spectra. Similarly, May *et al.* (2013) grouped Late Mississippian–Cretaceous samples from the Big Horn Basin into four tectonostratigraphic assemblages, also based on their U–Pb age spectra.

Breakpoint analysis proceeds as described by Saylor *et al.* (2019) and is summarized here. We first plot the final residual v. the rank and apply a segmented linear regression with one break. We calculate the sum of squared residuals (*SSR*; Draper and Smith

1998) for each segment as

$$SSR_1 = \sum_{r=2}^{r=x_b} (R_r - f(x_r))^2 \quad (3)$$

and

$$SSR_2 = \sum_{r=x_b}^{r=n} (R_r - (g(x_r))^2. \quad (4)$$

In these equations x_b is the breakpoint, which is calculated for all integers between 2 and n, where n is the maximum rank being considered. R_r is the final residual for each rank (r), and $f(x_r)$ and $g(x_r)$ are the expected final residual calculated by linear regression over the lower-rank or higher-rank segments, respectively. For $x_b = 2$ and $x_b = n$, $f(x_b)$ and $g(x_b)$ are equal to the final residual, yielding SSR_1 and $SSR_2 = 0$, respectively. The optimal rank is then the x_b that minimizes the sum $SSR_1 + SSR_2$.

Bi-cross-validation proceeds following the algorithm developed by Owen and Perry (2009). We divided the input matrix V from Equation (1) (with dimensions $i \times j$) into four quadrants as follows:

$$V = \begin{bmatrix} A & B \\ C & D \end{bmatrix}, \quad (5)$$

where $A \in R^{r \times s}$, $B \in R^{r \times (j-s)}$, $C \in R^{(i-r) \times s}$, and $D \in R^{(i-r) \times (j-s)}$. We then conducted NMF on all quadrants (A, B, C, D) for all ranks from $k = 2$ to $k = n$ and used the factorized matrix to calculate the residual of the matrix on its diagonal. Hence, $D = \widehat{W}_D^k \widehat{H}_D^k$ is the NMF of quadrant D for rank k and is used to calculate the residual for A in Equations (6–8) below. We calculated the residual difference (R_A^k) between the factorized matrices and their known counterparts as the Frobenius norm of

$$A - \widehat{W}_A^k \widehat{H}_A^k, \quad (6)$$

where

$$\widehat{W}_A^k = B\widehat{H}_D^{+k}, \quad (7)$$

$$\widehat{H}_A^k = \widehat{W}_D^{+k} C. \quad (8)$$

In this scenario the optimum rank is the k that minimizes the residual R. We also considered the rank that minimizes the sum of residuals $R_{tot} = R_A + R_B + R_C + R_D$.

Synthetic data sets

We first tested the method on three numerically generated bivariate data sets. Inputs to the NMF algorithm were comprised of 24–40 samples of paired U–Pb and εHf_T data mixed from three, five, or eight known sources. Mixing was done by first assigning a random weight to each of the sources using the randomization algorithm of Sundell and Saylor (2017). Age and εHf_T pairs were then drawn from each of the sources in proportion to their randomly assigned weight. Factorization of the data sets with three and five sources proceeded similarly to that with eight sources (Supplemental Tables S1–S6). Therefore, for brevity we discuss the data sets with eight sources below, while the others are fully discussed in the Supplemental text.

Eight sources were derived from a global database of U–Pb and εHf_T data from igneous zircons compiled by Puetz and Condie (2019) (Fig. 2a and Supplemental Tables S7 and S8). We divide the data set into eight continental land masses following the Paleozoic suture boundaries identified by Domeier and Torsvik (2014). These include Africa (n = 4882), Antarctica (n = 2084), Asia (n = 14 881), Australia (n = 4654), Baltica (n = 2115), North America (n = 4264), South America (n = 3948), and a suite of peri-Gondwanan terranes (n = 10 289). We mixed these eight sources into 40 sinks where all sink samples have 2084 age/εHfT pairs.

Quantitative comparison

We applied two statistical measures to compare the reconstructed sink samples to known sink samples and factorized sources to known sources. The first is the cross-correlation coefficient as applied in provenance studies (Saylor *et al.* 2012, 2013; Saylor and Sundell 2016; Sundell and Saylor 2021). This is applied to pairs of two-dimensional KDEs by comparing all elements of a square matrix (i.e. $m \times m$) which represents KDE_1 with the corresponding elements of KDE_2. For computational efficiency each matrix is vectorized ($KDE_1^{m \times m} \rightarrow V_1^{m^2 \times 1}$ where V_1 has dimensions $m^2 \times 1$), and the cross-correlation coefficient is then calculated using the

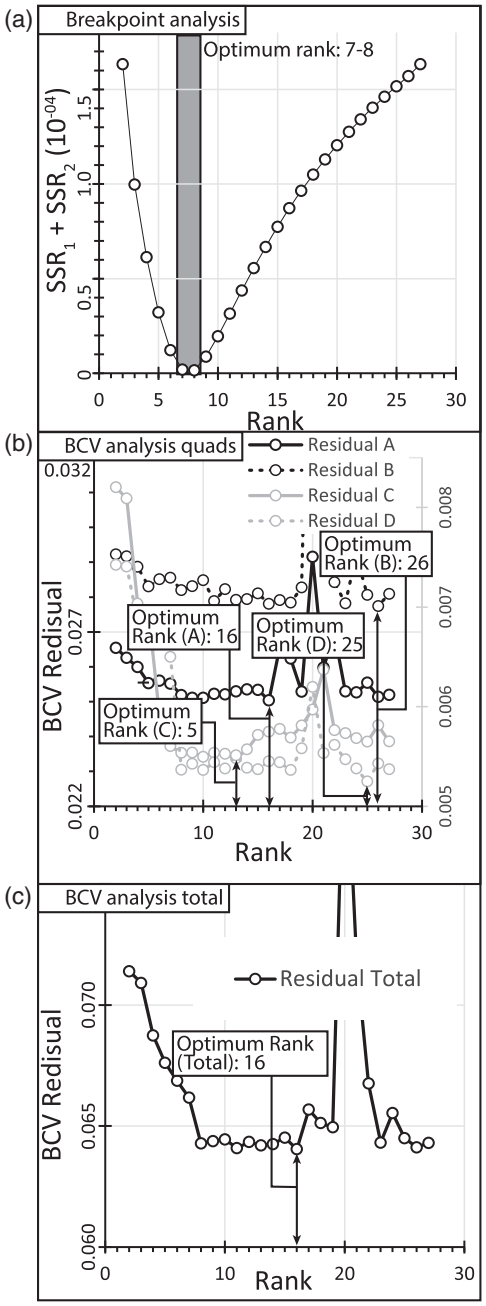

Fig. 3. (**a**) Breakpoint analysis based on factorization of 40 sink samples from eight sources to ranks between 2–27 yields a minimum sum of squared residuals at rank eight, closely followed by rank seven. (b) Bi-cross-validation of based on factorization of four quadrants (i.e. A, B, C, D in equation (5)) from the 40 sink samples for ranks 2–27 yields minima in residual at ranks ranging from 5 to 26. (c) The sum of residuals of each of the four quadrants yields a minimum at a rank of 16. Data for this figure are presented in Supplemental Table S9.

standard equation

$$R^2 = \left(\frac{\sum_{i=1}^{m^2} (V_1(i) - \overline{V_1}) * (V_2(i) - \overline{V_2})}{\sqrt{\sum_{i=1}^{m^2} (V_1(i) - \overline{V_1})^2 * \sum_{i=1}^{m^2} (V_2(i) - \overline{V_2})^2}} \right)^2 . \quad (9)$$

The second statistical measure is the Kolmogorov–Smirnov distance (D value). Unfortunately, unlike the univariate case, the cumulative distribution function (CDF) is not uniquely defined in more than one dimension. We therefore follow Peacock (1983) and Press and Teukolsky (1988) in calculating the D value for each quadrant surrounding each point in two two-dimensional CDFs. The final D value is then the maximum D value calculated from each quadrant (see Sundell and Saylor 2021, for further discussion).

We also use multi-dimensional scaling (MDS) to visualize the relationship between the six factorized endmembers and the 29 potential empirical sources (Vermeesch 2013). MDS attempts to present the dissimilarity between samples as distance in *N*-dimensional space. Samples are represented as a point, typically in two- or three-dimensional Cartesian space, with greater distances between two points indicating greater dissimilarity between the two samples. The transformation is accomplished by iterative rearrangement of the data in *N*-dimensional space to minimize the misfit ('stress') between the calculated distances and the disparities. In a low-stress MDS plot, the distances between points linearly correlate to the dissimilarities between samples. MDS was conducted using the *DZmds* software package and optimized the metric squared stress based on the coefficient of non-determination (i.e. complement of the cross-correlation coefficient, $1–R^2$) (Saylor *et al.* 2017). Squared stress is calculated as

$$\left(\frac{\sum_{ij} (f(x_{ij})^2 - d_{ij}^2)^2}{\sum_{ij} d_{ij}^4} \right)^{0.5} , \quad (10)$$

where d_{ij} is the distance and $f(x_{ij})$ is the disparity between the *i*th and *j*th element. Disparity is calculated as a linear (1:1) transformation of the input dissimilarities.

Results

Rank estimation

For data sets randomly mixed from known sources, breakpoint analysis consistently yields optimum ranks within one of the known number of sources (Fig. 3a, Supplemental Figures S2A and S5A). In contrast bi-cross-validation yields different optimum ranks based on the residual for each of the four quadrants (i.e. A, B, C, D in Equation (5)) examined, as well as for the total residual (Fig. 3b and c, Supplemental Figures S2B–C and S5B–C). For example, breakpoint analysis of the 40 sink samples mixed from eight sources indicates that the optimum rank for factorization is eight, although rank seven is only slightly worse (Fig. 3a, Supplemental Table S9). In contrast, bi-cross-validation yields a range of optimum ranks between 5 and 26 (Fig. 3b) for the individual quadrants. The total residual indicates that the optimum rank is 16 (Fig. 3c).

Bivariate distributions and mixture weights

Since breakpoint analysis indicates that a rank of either seven or eight yields optimum factors (Fig. 3a), we factorized the 40 sink samples mixed from eight sources to both seven and eight endmembers (Fig. 2b and c). The cross-correlation coefficient and D value indicate close similarity between the known sources to both seven and eight endmembers factorized from the mixed sink samples. However, there is a slightly better match between the endmembers factorized for rank eight than for rank seven (compare Fig. 2b and c). The mean cross correlation coefficient between factorized endmembers for rank eight and the known sources is 0.99. In comparison the mean cross-correlation coefficient between factorized endmembers for rank seven and the known sources is 0.96, or 0.93 if the best match to Input 5 is included (Fig. 2c).

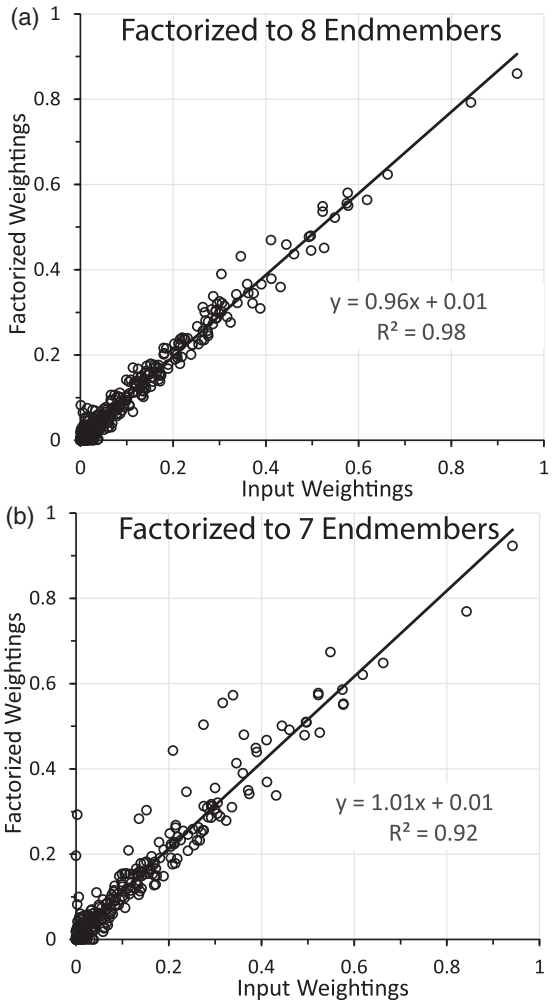

Fig. 4. Comparison of the known weights for the 40 sink samples mixed from eight known sources to the mixing weights based on factorization of the sink samples. (**a**) Comparison based on factorization to rank eight. (**b**) Comparison based on factorization to rank seven. For factorization to rank seven the comparison is based on the weightings for the seven factorized sources that most closely match the known counterparts (see Fig. 2c). Data for this figure are presented in Supplemental Table S9.

There is close correspondence between the mixture weighting used to mix the eight sources into 40 sink samples and the weightings based on factorization of the 40 sinks (Fig. 4). Cross-plotting mixture weights from the factorization to rank eight and known mixture weights yields a linear fit with a slope of 0.96 and a coefficient of determination of 0.98 (Fig. 4a). Cross-plotting mixture weights from the factorization to rank seven and known mixture weights yields slightly lower coefficient of determination (0.92), but a linear fit with a slope (1.01) which is closer to 1 than the slope for rank eight (Fig. 4b).

Empirical data set

As a second test of the algorithm as applied to an empirical data set, we factorized 24 Neoproterozoic–Triassic U–Pb and εHf_T data sets from basins spanning central and western North America (Figs 5 and 6) (Wooden *et al.* 2013; Gehrels and Pecha 2014; Linde *et al.* 2016, 2017; Thomas *et al.* 2020). We compared the results of this factorization to 29 potential sources in order to assess whether factorization of empirical samples results in recovery of plausible

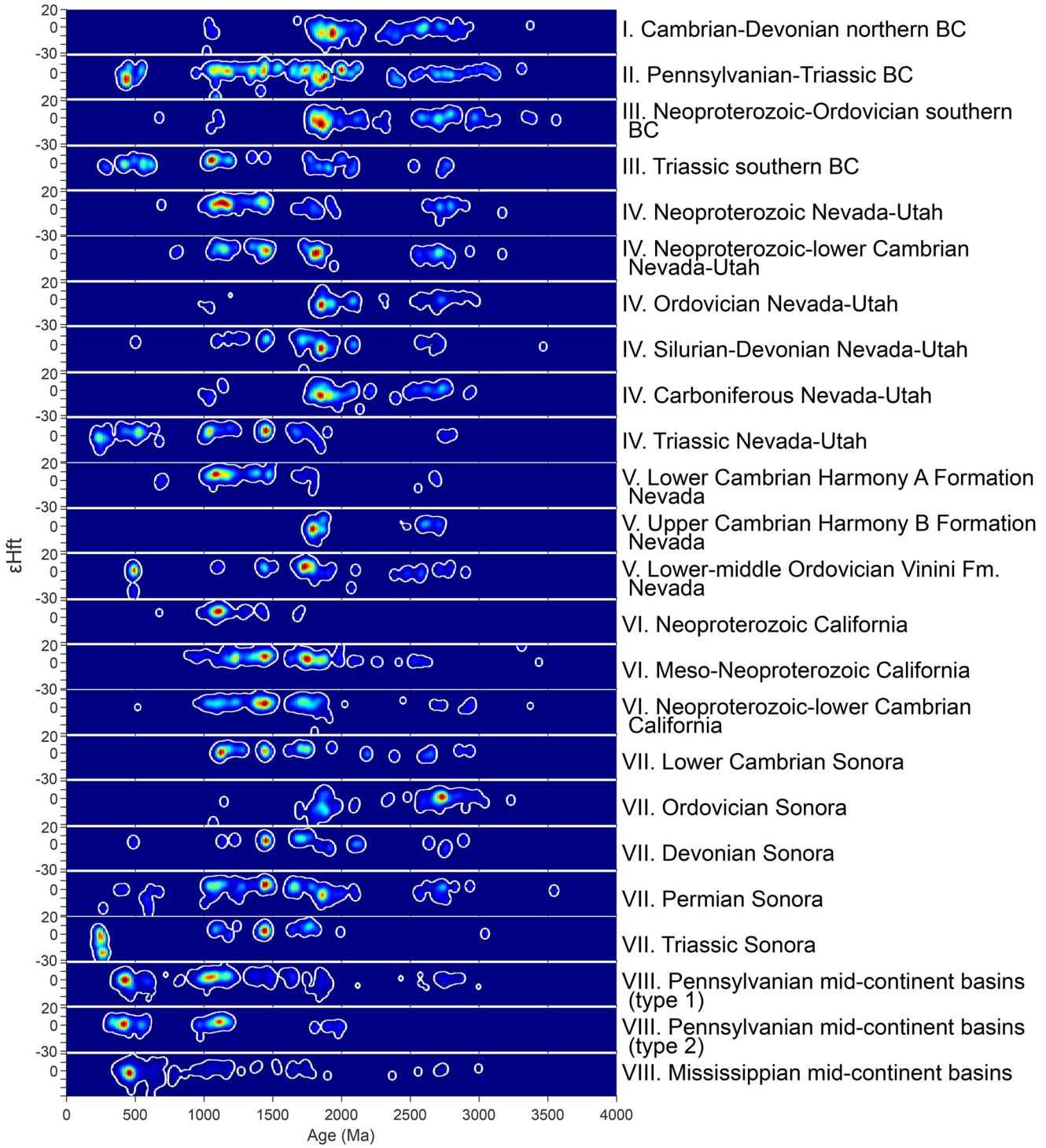

Fig. 5. Zircon U–Pb age and εHf_T data sets from Neoproterozoic–Triassic samples from basins spanning central–western Laurentia. Factorization of these samples forms the basis for the paleogeographic reconstruction in Figure 10. White contour lines are plotted at the median (50th percentile). Roman numerals are keyed to locations in Figure 6. The data in this figure are presented in Supplemental Table S10.

bivariate distributions (Figs 5 and 6 and Supplemental Table S7) (Andersen *et al.* 2002, 2007, 2011; Bickford *et al.* 2008; Mueller *et al.* 2008; Røhr *et al.* 2008, 2010; Flowerdew *et al.* 2009; Appleby *et al.* 2010; Bickford *et al.* 2010; Rehnström 2010; Stewart *et al.* 2010; Weber *et al.* 2010; Brander *et al.* 2011; Anfinson *et al.* 2012; Augland *et al.* 2012; Malone 2012; Cochrane 2013; Doe *et al.* 2013; LaFlamme *et al.* 2013; Willner *et al.* 2013; Wooden *et al.* 2013; Holland *et al.* 2015; Pollock *et al.* 2015; Henderson *et al.* 2016; Thomas *et al.* 2017; Zirakparvar *et al.* 2017; Cecil *et al.* 2019). See Supplemental Table S10 for samples, sample groupings, and sources.

Breakpoint analysis indicates that the optimum factorization rank for the 24 Neoproterozoic–Triassic U–Pb and εHf_T data sets is six (Fig. 7). Factorization to rank six yields the distributions shown in Figure 8a. Endmember 1 is characterized by U–Pb ages between 200–300 Ma and εHf_T values ranging from 10 to −30 coupled with Mesozoic–Paleoproterozoic U–Pb ages with εHf_T values >0 (Fig. 8a). Endmember 2 has similar Mesozoic–Paleoproterozoic U–Pb age distributions and associated positive εHf_T values but lacks the late Paleozoic–Mesozoic U–Pb ages (Fig. 8a). Endmember 3 is characterized by a positively skewed mode between 1.0–1.2 Ga and εHf_T values between 20 and −10 (Fig. 8a).

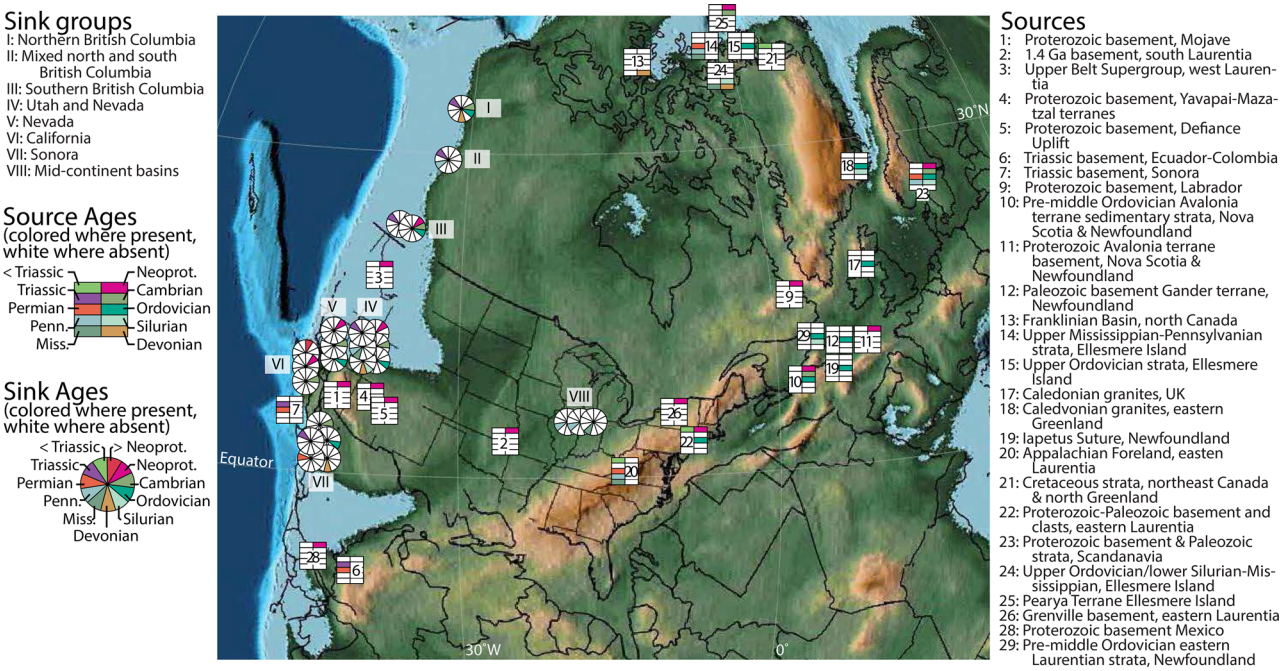

Fig. 6. Paleogeographic map of Laurentia at 250 Ma showing the location of sink samples used in factorization and empirical source samples that they are compared to. Maps are from the PaleoAtlas for GPlates (Scotese 2016; Müller *et al.* 2018).

Endmember 4 has a single primary U–Pb/εHf_T age mode between 1.75 and 1.8 Ga, which is characterized by a wide range of εHf_T values from 20 to −30, and a secondary mode at *c.* 2.6 Ga that has εHf_T values of 0 ± 10 (Fig. 8a). Endmember 5 has a primary early Paleozoic U–Pb age mode that has a range of εHf_T values from 20 to −30 and a secondary late Neoproterozoic mode with similar εHf_T values (Fig. 8a). Endmember 6 is dominated by a positively skewed U–Pb age mode at *c.* 1.8 Ga that displays a range of εHf_T values from 10 to −30. It has a secondary U–Pb age mode at *c.* 2.7 Ga with εHf_T values of 0 ± 10 (Fig. 8a).

Discussion

Synthetic data sets

Analysis of the synthetic data sets indicates that breakpoint analysis provides a more consistent optimum factorization rank than bi-cross-validation. The optimal rank yielded by bi-cross-validation ranged from *c.* 0.75 to more than three times the known number of sources (Fig. 3b, Supplemental Figures S2B and S5B). The optimal rank estimated by breakpoint analysis also more closely matches the known number of sources than the rank estimated by bi-cross-validation. The final optimal rank based on the sum of residuals from bi-cross-validation of the four quadrants was consistently double the known number of sources (Fig. 3c, Supplemental Figures S2C and S5C). In contrast, breakpoint analysis yielded consistent optimal ranks, and the optimal ranks were within one of the known number of sources (Fig. 3a, Supplemental Figures S2A and S5A).

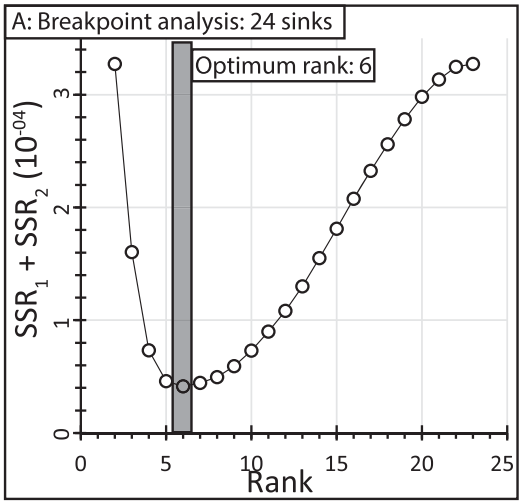

Fig. 7. Breakpoint analysis of 24 samples of Neoproterozoic–Triassic samples from the western USA and Canada yields an optimum rank of 6. Data for this table are presented in Supplemental Table S11.

Factorization to the optimum rank indicated by breakpoint analysis yields distributions and mixing weights that closely match the known distributions and mixing weights. For example, factorizing of the eight-source data set to seven or eight endmembers yields high mean cross-correlation coefficients (0.96–0.99). Similarly, for the eight-source data set the R^2 between known and factorized mixing weights is slightly higher for the eight-endmember factorization (0.98) than for the seven-endmember factorization (0.92) (Fig. 4).

These results indicate that NMF of bivariate data sets provides insight into the distributions and mixtures present in the data. We conclude that NMF of bivariate data sets is a reliable method to reconstruct both the distribution of characteristics of sediment sources and also the weighting of those sources in sink populations.

Empirical data set

Loci of potential sources

Neoproterozoic–Triassic strata from the western Laurentian margin, Ancestral Rocky Mountain basins, and mid-continent basins contain zircons with Archean–Triassic U–Pb ages (e.g. Gehrels *et al.* 2011; Kissock *et al.* 2018; Leary *et al.* 2020, and many others). Significant age ranges have multiple sources in basement provinces in Laurentia, as laid out below. In addition to direct derivation from these crustal domains, zircons could be recycled through sedimentary strata derived from the initial zircon source terrane. However,

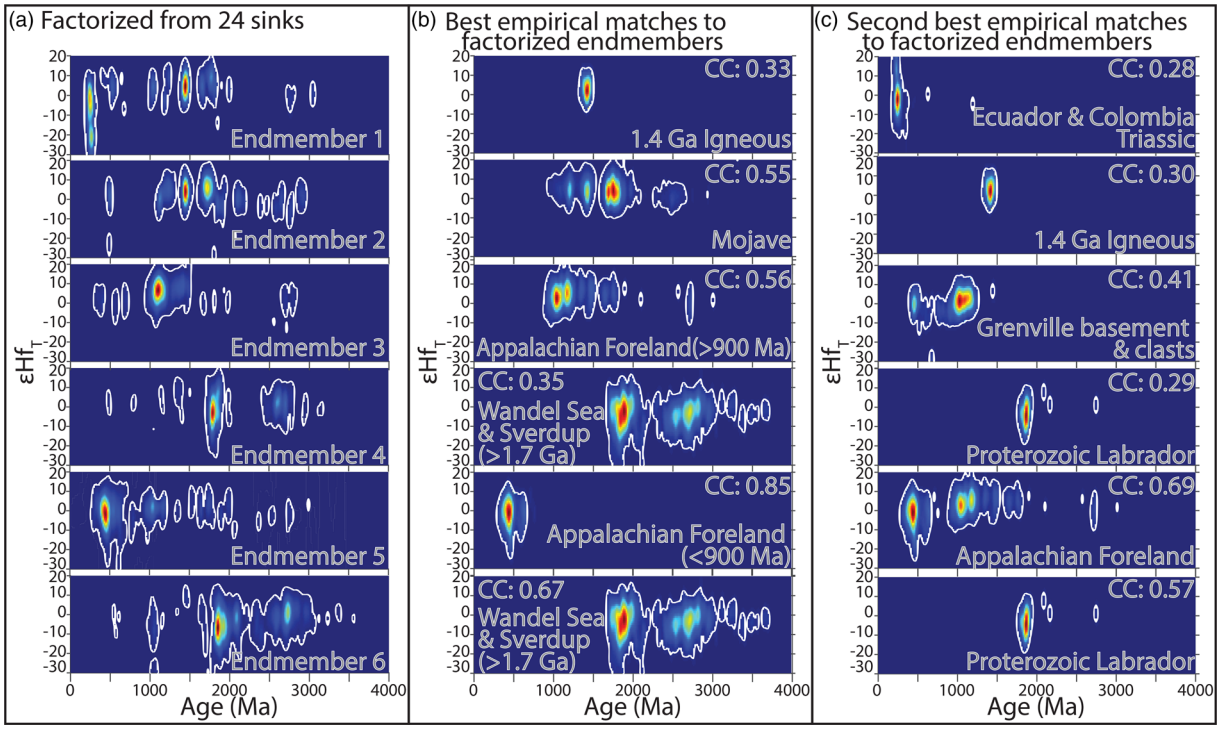

Fig. 8. Comparison between sources factorized from the Laurentian Neoproterozoic–Triassic data set and their closest and second-closest empirical correlatives. (**a**) Factorized endmembers. (**b**) Closest matches sorted by row and shown adjacent to the factorized endmembers that they match. (**c**) Second-closest matches sorted by row and shown in the same row as the factorized endmembers that they match. CC denotes the cross-correlation coefficient between the empirical source and the factorized endmember on the same row. Data for this figure are presented in Supplemental Table S10.

recycling is likely to mix sources in distinct proportions as described below in the section titled 'Sediment routing in Paleozoic Laurentia'. The difference in proportions is exploited by the NMF algorithm to factorize out both the age/εHf_T distributions and the mixing proportions. On the other hand, if an age/εHf_T distribution is dispersed homogeneously throughout the sink data set, the NMF algorithm will be unable to factorize that source into contributing components (see the discussion in Saylor *et al.* 2019; Smith *et al.* 2020).

Mesoarchean–early Paleoproterozoic (>2.4 Ga) zircons may be derived from cratonic provinces and intervening Proterozoic orogens and arcs of northern Laurentia (Percival *et al.* 2004). This includes the Superior (3.8–2.6 Ga; Hoffman *et al.* 1989; Percival *et al.* 2004), Slave (3.3–2.5 Ga; Bleeker *et al.* 1999; Ootes *et al.* 2005), Medicine Hat (3.3–2.5 Ga; Villeneuve *et al.* 1993; Gifford *et al.* 2020), Rae (3.4–2.3 Ga), and Wyoming provinces (3.5–2.5 Ga; Ross 2002; Chamberlain *et al.* 2003).

Early–middle Paleoproterozoic (*c.* 2.4–2.0 Ga) zircons are relatively rare in Laurentia, but have been reported in accreted terranes in northwestern Laurentia including the Tatlson Orogen, the Buffalo Head terrane, the Chinchaga Domain (Ross *et al.* 1991; Thériault and Ross 1991; Villeneuve *et al.* 1993; Ross 2002), and sedimentary strata derived from them (Partin *et al.* 2014; Shiels *et al.* 2017, and references therein). Early–middle Paleoproterozoic crystallization ages have also been reported from limited intrusions in the Slave, Rae, and Hearn cratons (e.g. Hartlaub *et al.* 2007; Mumford 2013).

Paleoproterozoic–early Mesoproterozoic (2.0–1.6 Ga) zircon U–Pb ages may be from the Yavapai–Mazatzal terrane of southwestern Laurentia, basement of Greenland and Scandanavia (Hoffman 1988; Kalsbeek *et al.* 1993, 2008; Fonneland *et al.* 2004; Nutman *et al.* 2008; Gehrels *et al.* 2011; Slama *et al.* 2011; McClelland *et al.* 2016; Linde *et al.* 2017), and also orogens and arcs of the northern Laurentian Wopmay Orogen (1.8–1.9 Ga and 2.5–2.7 Ga) (Jackson *et al.* 2013). Similarly, zircons from the Mojave crustal block of southwestern Laurentia have crystallization ages of *c.* 1.8–1.4 Ga (Wooden *et al.* 1988; Hawkins *et al.* 1996; Barth *et al.* 2000). Depleted mantle Nd model ages and inherited zircon ages of 2.3–2.0 Ga in Mojave province granites indicate incorporation of older crustal material (Hawkins *et al.* 1996; Barth *et al.* 2000).

Late Mesoproterozoic ('Grenville') zircons have a wide variety of potential sources. These include Gondwanan terranes in the northern Appalachian Orogen, and exposed and subsurface sources in the Grenville Province of eastern and southern Laurentia (Percival *et al.* 2004; Fyffe *et al.* 2009; Macdonald *et al.* 2014; Karabinos *et al.* 2017; Thomas *et al.* 2017; Kissock *et al.* 2018). Alternatively, they have been attributed to the Ellesmerian Orogen and clastic wedge based on statistical similarity (Leary *et al.* 2020), Proterozoic basement of central Mexico (Weber *et al.* 2010), Gondwanan and peri-Gondwanan sources accreted to southern Laurentia (Liu and Stockli 2019), or Scandinavian Paleozoic strata and Proterozoic basement (Andersen *et al.* 2007, 2011, 2014; Brander *et al.* 2011; Augland *et al.* 2012; Kristoffersen *et al.* 2014).

Zircons with late Neoproterozoic (Cryogenian–Ediacaran)–early Paleozoic ages have been attributed to peri-Gondwanan terranes accreted to Laurentia during the assembly of Pangea (Kissock *et al.* 2018), subduction-related magmatism on the eastern and northeastern margin of Laurentia (Rehnström 2010), and Iapetan syn-rift rocks exposed in the northern Appalachian Orogen (Thomas 2014). Within this group, Cambrian-aged zircons have been attributed to sources ranging from the Amarillo–Wichita Uplift, to peri-Gondwanan terranes, or isolated Cambrian granites in New Mexico and Colorado (McMillan and McLemore 2004; Martens *et al.* 2010; Thomas *et al.* 2016). Finally, Permo-Triassic magmatism occurred along the western margin of Laurentia and even into northern South America (Riggs *et al.* 2016; Cecil *et al.* 2019).

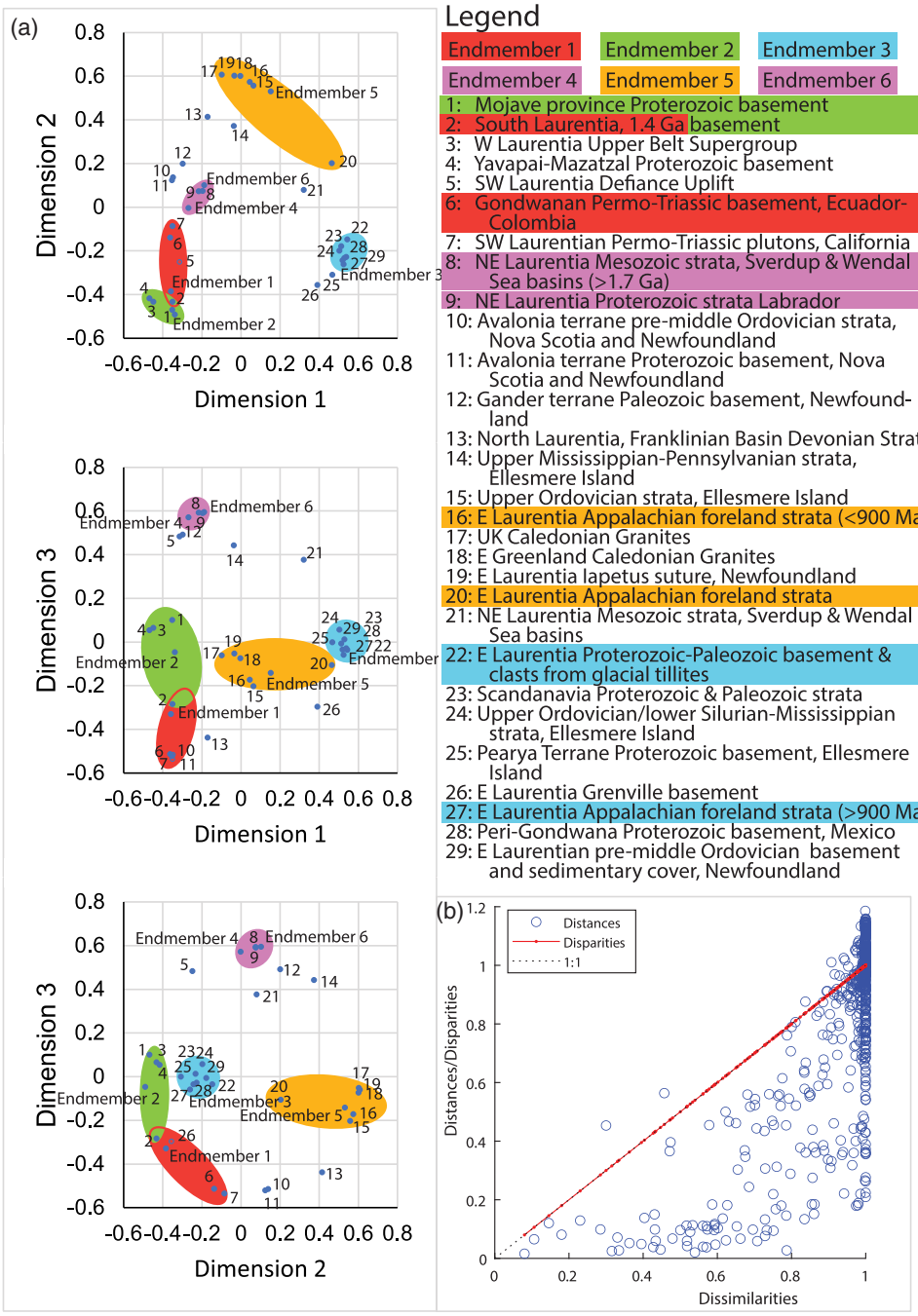

Fig. 9. Three-dimensional multi-dimensional scaling of the 29 potential empirical sources and six factorized sources based on minimizing metric squared stress of the cross-correlation coefficient. (**a**) Each panel shows two axes of the three-dimensional projection. Unfilled data points indicate samples that appear to be part of a group but can be seen as distinct upon examination of the third dimension. (**b**) Shepard plot. Stress is 0.36. Data for this figure are presented in Supplemental Table S12.

Comparison of factorized and empirical sources

Three-dimensional MDS enables a broad evaluation of the groups of samples that most closely approximate factorized endmembers (Fig. 9). Although the MDS plot yields coherent groupings we treat the results with caution because the final stress is relatively high (0.36). Numbers following source descriptions in this paragraph refer to the legend of Figure 9. Endmember 1 is closely correlated to zircons from the 1.4 Ga 'anorogenic' granite province (2), or Permo-Triassic plutons in Ecuador and Colombia (6) or the Mojave province of California (7). Endmember 2 is correlated to zircons from igneous and metamorphic basement rocks of the Mojave terrane (1), the 1.4 Ga 'anorogenic' granite province (2), Mesoproterozoic strata of the Belt Supergroup from Idaho and Wyoming (3), and igneous and metamorphic basement rocks of the Yavapai and Mazatzal terranes (4). Endmember 3 has multiple correlations in eastern and northern Laurentia (22, 24, 25, 27, 29), Scandinavia (23), and central Mexico (28). Endmembers 4 and 6 are most closely correlated to the >1.7 Ga age/εHf_T distributions from the Severdup and Wendal Sea basins (8) or Paleoproterozoic metavolcanics and metaigneous rocks from Labrador (9). Endmember 5 correlates to Paleozoic strata from the Appalachian foreland basin (16, 20), Ordovician strata deposited on the Pearya Terrane (Ellesmere Island) prior to its accretion to northern Laurentia (15), Caledonia granites exposed in the UK (17) and eastern Greenland (18), and sedimentary strata along the Iapetus exposed in Nova Scotia (19).

Given the high stress associated with the MDS plot, we identify the closest matches to the six endmembers based on the cross-correlation coefficient in order to further hone our interpretation (Figs 8 and 10). Endmember 1 is most closely correlated to zircons from the 1.4 Ga 'anorogenic' granite province, and secondarily to Triassic plutons in Ecuador and Colombia. Endmember 2 is best matched by zircons from igneous and metamorphic basement rocks of the Mojave terrane, with the 1.4 Ga 'anorogenic' granite province providing a second-best match. The closest match to Endmember 3

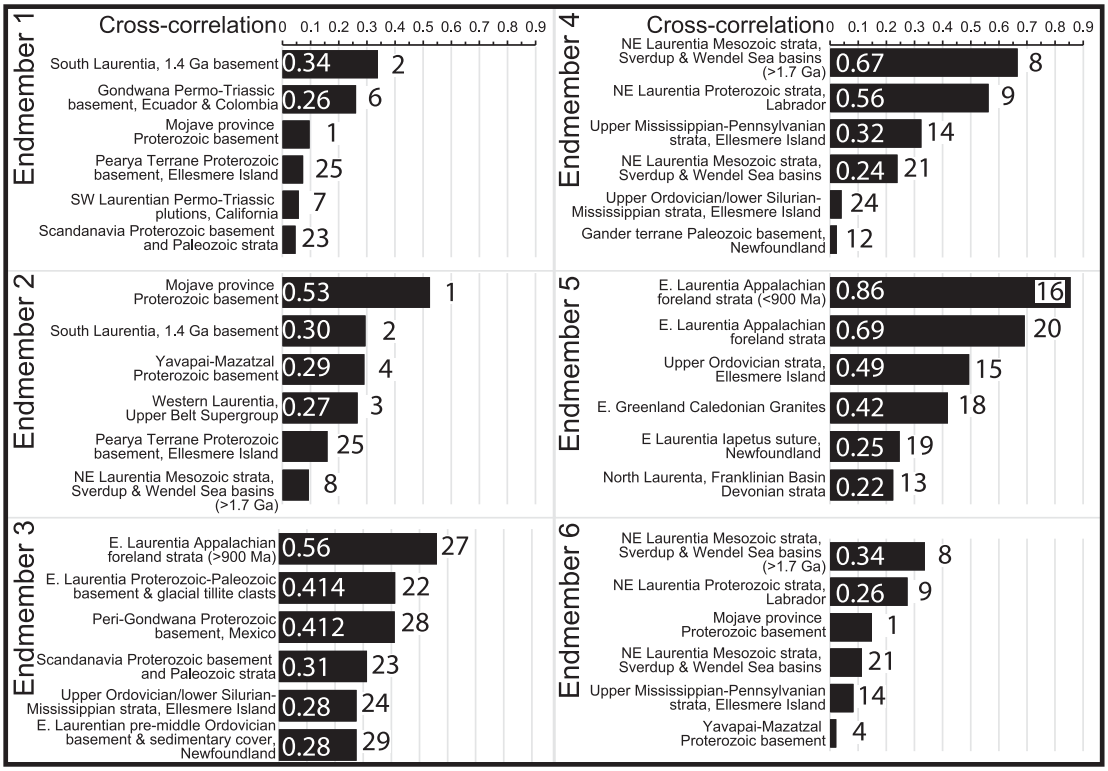

Fig. 10. Comparison of the six factorized endmembers and their six closest empirical matches, ranked by cross-correlation coefficient. White numbers inside bars indicate the associated cross-correlation coefficient for clarity. Black numbers adjacent to histogram bars refer to sources identified in Figure 9. Data for this figure are presented in Supplemental Table S12.

is the >900 Ma distribution of ages and εHf_T values from Paleozoic Appalachian foreland strata. Endmember 3 has a secondary match to Proterozoic basement and igneous clasts from glacial till from New York. Both Endmembers 4 and 6 are most closely correlated to the >1.7 Ga age/εHf_T value distributions from the Sverdup and Wandel Sea basins and secondarily to Paleoproterozoic basement from Labrador. Finally, Endmember 5 is best matched either by the <900 Ma age/εHf_T value distribution from Paleozoic strata of the Appalachian foreland or the entire distribution from the same strata.

Sediment routing in Paleozoic Laurentia

Factorization of 24 Neoproterozoic–Triassic sample groups from central–western Laurentia yields endmembers that match known potential sources on the southern, eastern and northern margins of Laurentia. This broadly supports previous interpretations of late Paleozoic sediment transport (Gehrels *et al.* 2011; Gehrels and Pecha 2014; Chapman and Laskowski 2019; Leary *et al.* 2020; Thomas *et al.* 2020) but refines previous source attributions and hence paleogeographic reconstructions. Zircon proportions in basin strata are a function of the volume of rock eroded, but also the lithology and zircon fertility of that rock, weathering, sediment flux, sorting during transport, sediment transport mechanism, and sampling and processing procedures (Moecher and Samson 2006; Key *et al.* 2012; Sláma and Košler 2012; Malusà *et al.* 2013, 2016; Lawton *et al.* 2015; Ibañez-Mejia *et al.* 2018; Malkowski *et al.* 2019; Pettit *et al.* 2019). As a result, we treat proportions in the discussion below with caution, relying primarily on whether samples indicate a single dominant source or multiple sources. In the discussion below all coordinates are given in a modern reference frame.

Proterozoic–Early Cambrian. Factorization of Proterozoic–lower Cambrian samples from southern and northern British Colombia yields sources consistent with derivation from the same sources that shed detritus to the Mesozoic Sverdup and Wandel Sea basins (Røhr *et al.* 2008, 2010) and that match Proterozoic basement sources in Labrador and Newfoundland (LaFlamme *et al.* 2013). We interpret this as reflecting a sediment dispersal system that traversed northern Laurentia in a roughly east–west direction (Fig. 11a and b). With this dataset we cannot rule out the possibility of deposition in and recycling from intermediate depocenters. Likewise, factorization of samples from California, Nevada–Utah and Sonora are consistent with derivation from the same sources that later shed sediment to the Appalachian foreland basin (Fig. 8a, Endmember 3). We interpret this as reflecting an east–west transcontinental sediment routing system that delivered sediment from the Grenville basement of eastern Laurentia to western and southwestern Laurentia (Fig. 11a and b). These samples also indicate derivation from local sources in the Mojave province (Fig. 8a, Endmember 2).

The east–west transcontinental sediment dispersal indicated by this combination of sources and sinks is at odds with the conclusion of Gehrels and Pecha (2014) that the Transcontinental Arch formed a topographic barrier to westward sediment dispersal across the mid-latitudes of Laurentia. However, it provides support for a similar scenario of transcontinental sediment transport proposed by Linde *et al.* (2017). Furthermore, these conclusions are consistent across six (of seven) Mesoproterozoic–early Cambrian data sets from southwestern Laurentia (Fig. 11a and b), suggesting that the model results and application to bivariate data are robust. We conclude that this is an instance where quantitative modeling and comparison of bivariate data sets is able to refine and quantitatively assess sediment provenance and so provide objective discrimination between competing hypotheses.

Late Cambrian–Ordovician. There is a marked change in sediment source for samples from southwestern Laurentia (including Nevada–Utah and Sonora) during this interval. Factorized sources for the majority of the samples from western

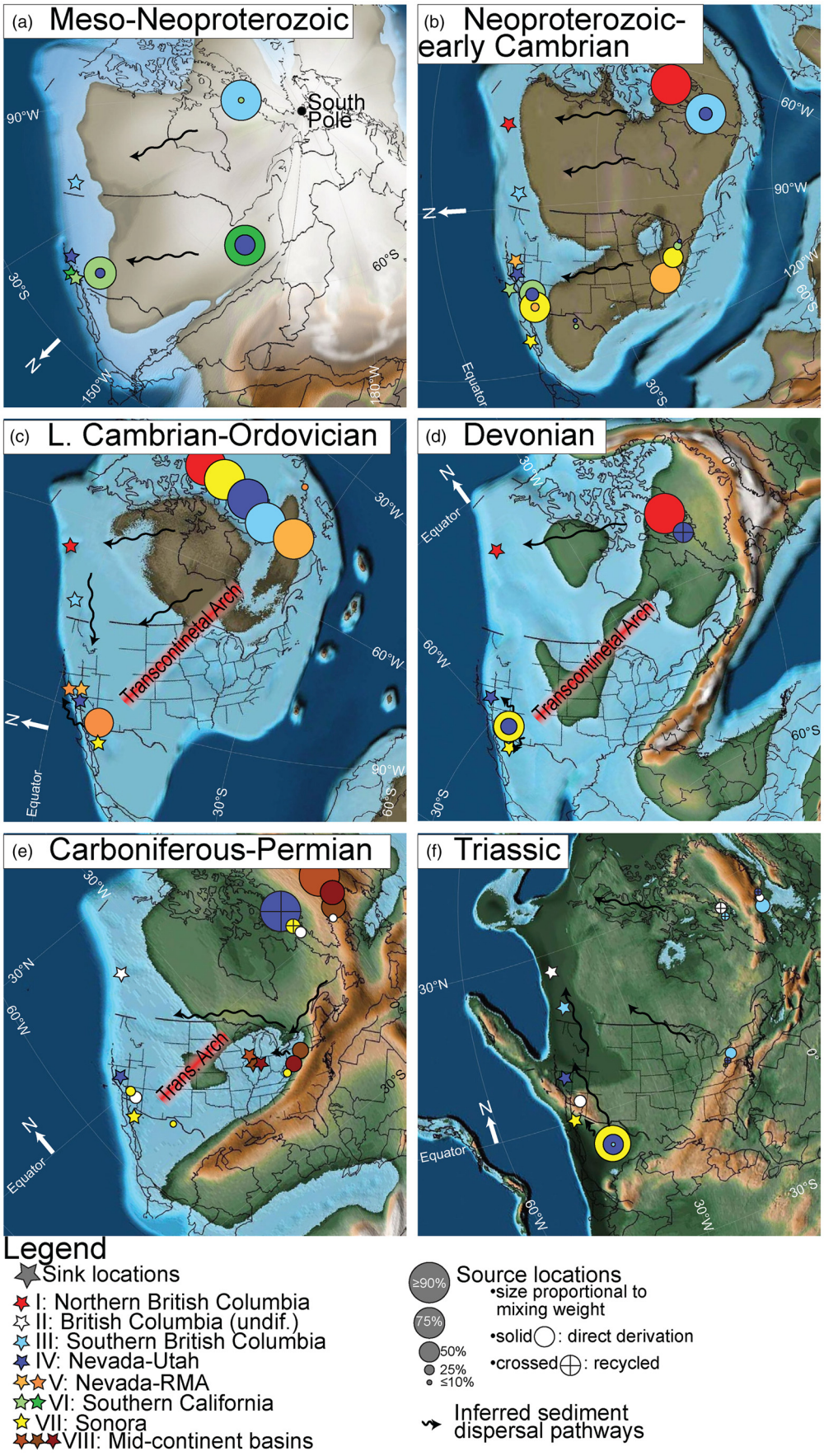

Fig. 11. Paleogeographic maps of Laurentia from Neoproterozoic through Triassic time showing the location of sediment sinks (stars), sources (circles) and inferred sediment transport pathways (black lines and arrows). Circles are scaled based on the mixing weight estimated by non-negative matrix factorization. All maps are oriented in their modern spatial frame with north at the top of the figures. (**a**), (**b**) In the Mesozoic–Neoproterozoic and Neoproterozoic–Lower Cambrian timeslices factorization yields sources consistent with those in eastern Laurentia, suggesting transcontinental sediment transport. Samples in southwestern Laurentia also indicate derivation from local sources. (**c**) In the late Cambrian–Ordovician timeslice all sink sample models are dominated by

sources in northeastern Laurentia. (**d**) In the Devonian timeslice, models of samples in British Columbia are consistent with derivation from northeastern Laurentia. In contrast, models of samples from southwestern Laurentia indicate a combination of local and northeastern sourcing. We infer that this combination reflects local recycling of Cambrian–Ordovician strata and therefore that southwestern Laurentia was largely isolated from transcontinental sediment transport in the Devonian. (**e**) The Carboniferous–Permian timeslice shows reintegration of transcontinental drainage across southern Laurentia, with samples in southwestern Laurentia indicating renewed derivation from the same Grenville basement and northeastern Laurentian sources as samples from mid-continental basins. (**f**) The Triassic time timeslice shows that sediment dispersal had largely reorganized with sediments being shed from south to north. Maps are from the PaleoAtlas for GPlates (Scotese 2016; Müller *et al.* 2018). Data for this figure are presented in Supplemental Table S13.

Laurentia are consistent with the derivation from sources that shed sediment into the Mesozoic Sverdup and Wandel Sea basins (Røhr *et al.* 2008, 2010), and basement sources in Labrador and Newfoundland (LaFlamme *et al.* 2013) (Fig. 8a, Endmembers 4 and 6). This implies large-scale southward or southwestward sediment transport and is likely a response to the onset of the Taconic phase of the Caldonian Orogeny (Fig. 11c) (McKerrow *et al.* 2000; van Staal *et al.* 2009). We follow previous authors in concluding that sediment was dispersed via a combination of westward fluvial and southward long-shore current transport (Chapman and Laskowski 2019; Leary *et al.* 2020). The exception to these transport pathways is the Vinini Formation (Nevada) which is largely attributed to sources in the Mojave province (Fig. 8a, Endmember 2), and suggests a northward sediment transport pathway. Consistent with emergence of the Transcontinental Arch as a topographic feature between the lower and upper Cambrian (Linde *et al.* 2017), NMF identifies no significant contribution of detritus attributable to eastern Laurentia in western Laurentian samples at this time (Fig. 11c).

Devonian. Detrital zircon data point to continued westward shedding of sediment from both northern and southwestern Laurentia. Samples from northern British Columbia continue to be dominated by a similar source as in the upper Cambrian–Ordovician (Fig. 8a, Endmembers 4 and 6). While this data set is compatible with either direct derivation from northern Laurentia or recycling Cambrian–Ordovician strata, the lack of mixing suggests direct derivation (i.e. little or no recycling). In comparison, samples from Nevada–Utah are mixtures of multiple sources, pointing to recycling of underlying strata. The simple distributions of samples from Sonora suggests direct derivation from local basement sources (Fig. 8a, Endmember 2). Thus, in southwestern Laurentia the mixture of sources attributed to northern Laurentia with local, Mojave block basement suggests that both the local basement and overlying strata were eroded and deposited in adjacent basins (Fig. 11d).

Carboniferous–Permian. The Carboniferous–Permian saw orogenesis on all margins of Laurentia as well as intraplate deformation in the Ancestral Rocky Mountains (e.g. Leary *et al.* 2017). Sediment provenance reflects this complexity and our conclusions are correspondingly tentative given our small sample size. Samples from southwestern Laurentia continue to reflect a mixture of multiple sources including northeastern Laurentia, Mojave block, and 1.4–1.5 Ga magmatic sources (Fig. 8a, Endmembers 1, 2, 4 and 6). We follow previous interpretations and attribute this signal to extensive recycling of strata on the western margin of Laurentia in response to Ancestral Rocky Mountain orogenesis and recycling of Roberts Mountain Allochthon or Antler foreland basin strata (Gehrels and Dickinson 2000; Gehrels and Pecha 2014; Linde *et al.* 2017).

Nevertheless, Mississippian strata from Arizona (Gehrels *et al.* 2011), Permian strata from Sonora (Gehrels and Pecha 2014), and Carboniferous strata from mid-continental basins (Thomas *et al.* 2020) record an influx of zircons with ages of 1.0–1.2 Ga and juvenile–evolved εHf_T values. NMF suggests that these are derived from sources that delivered sediment to the Appalachian foreland basin, and mid-continental basins (Fig. 8a, Endmember 3) (Thomas *et al.* 2017, 2020). With regard to basement lithologies, this source is most similar to basement and clasts from glacial tillites in New York (Zirakparvar *et al.* 2017). Samples from Laurentian mid-continental basins and British Columbia have age/εHf_T distributions that are similar to the <900 Ma portion of the age/εHf_T distribution from Appalachian foreland basin strata (Thomas *et al.* 2017) (Fig. 8a, Endmember 5). With regard to basement sources, this source is most similar to Caledonian granites in eastern Greenland (Rehnström 2010).

The presence of zircons with ages of 1.0–1.2 Ga and juvenile–evolved εHf_T values (Fig. 8a, Endmember 3) in Arizona, Sonora, and the mid-continental basins is consistent with the hypothesis that the sediment routing systems had buried and/or bypassed the Transcontinental Arch (Fig. 11e). An alternative interpretation is local derivation: on the western margin of Laurentia via recycling from underlying pre-Devonian strata, and in the mid-continental basins directly from Grenville crust. Following previous research, and for the reasons below, we favor the hypothesis that at least some sediment was transported from eastern to western Laurentia and represents re-integration of a transcontinental sediment transport system in southwestern Laurentia (Gehrels *et al.* 2011; Chapman and Laskowski 2019; Leary *et al.* 2020).

The Carboniferous–Permian interval saw the appearance of a source with a major Neoproterozoic–early Paleozoic age mode and juvenile–evolved εHf_T values (Fig. 8a, Endmember 5) in mid-continental basins and British Columbia. This source is closely matched by the <900 Ma portion of the distribution from Appalachian foreland basin strata and also Caledonian granites from eastern Greenland. At the same time, a portion of the distribution from Sonora is attributed to the same source that delivered sediment to the Appalachian foreland basin and mid-continental basins (Fig. 8a, Endmember 3) (Thomas *et al.* 2017, 2020), and is similar to basement and clasts from glacial tillites in New York (Zirakparvar *et al.* 2017). These sources are not present in pre-Devonian strata of either Sonora or British Columbia (Fig. 11e), suggesting that they were introduced for the first time in the Carboniferous–Permian via transcontinental transport. As has been highlighted by previous research, this interval represents an overtopping and/or bypass of the Transcontinental Arch and re-initiation of major sediment delivery from central eastern to western Laurentia (Chapman and Laskowski 2019).

Triassic. Triassic strata record a reorganization of sediment dispersal from southwestward to northwestward (Lawton 1994; Dickinson and Gehrels 2008). Mixture weights of Triassic samples in Sonora, Nevada–Utah and British Columbia indicate contributions from Endmember 1 (Fig. 8a). This source is mostly matched by 1.4–1.5 Ga basement from southern and central Laurentia (Fig. 10). Its second closest match is to highly evolved Permo-Triassic sources from Colombia and Ecuador (Cochrane 2013). There is a greater proportion of this source in Sonoran samples than in samples from Nevada-Utah, and it constitutes only a minor percentage of the zircons in samples from southern British Columbia. The northward dilution of this source is consistent with it being located in southwestern Laurentia or northwestern Gondwana (i.e. modern Colombia and Ecuador) and progressive dilution during northward transport (Fig. 11f).

Quantitative comparison between Endmember 1 and potential empirical sources identifies Permo-Triassic sources in northwestern Gondwana, rather than the more juvenile Permo-Triassic granitoids

or associated volcanism of the Mojave region (Riggs *et al.* 2016; Cecil *et al.* 2019), as the closest known match. This leaves two interpretive possibilities. First, at a minimum it requires relocating the source for Triassic strata away from the early Cordilleran arc of southern California and northern Mojave region to somewhere else. Based on the reasoning above, we suggest that potential sources should be sought to the southeast. Second, if the northwestern Gondwanan provenance is confirmed by future analyses, this conclusion requires defining a non-marine sediment distribution system that could transport sediment from Gondwana to Laurentia. In either case, this represents an instance where bivariate modeling and quantitative comparison can significantly revise sediment source identifications and therefore sediment dispersal pathways.

Summary. Several revisions of previous interpretations can be made based on NMF of the bivariate data sets. This includes attribution of Proterozoic–lower Cambrian detritus to east–west sediment dispersal, supporting a model in which the Transcontinental Arch did not emerge as a barrier to east–west transport until the late Cambrian (cf. Gehrels and Pecha 2014; Linde *et al.* 2017). Similarly, derivation of upper Cambrian–Ordovician detritus from western Laurentia as indicated by the bivariate data set confirms previous interpretations of SSW-directed sediment dispersal. Finally, attribution of Permo-Triassic zircons to a source in Gondwana revises previous source attributions.

The results of this study set the stage for interpretation of provenance records in the Jurassic–Paleogene retroarc foreland basin. First, we demonstrate that NMF can identify sediment sources in transcontinental sediment transport systems and we can therefore anticipate success applying this method to foreland basin strata. Second, recognizing these sources and their distribution in Proterozoic–Triassic strata on the western Laurentian margin provides a framework in which to interpret Jurassic–Paleogene provenance data. Particularly, the ability to discriminate zircons that are attributable to Yavapai–Mazatzal basement or Belt Supergroup strata from those attributable to northern or northeastern Laurentian sources suggests that these differences can be discriminated as they are recycled into younger foreland basin strata.

Software availability

We have developed an open-source software package for one-dimensional and two-dimensional NMF of detrital provenance data sets: *DZnmf2D*. This package is developed as a graphical user interface that can be run in a MATLAB environment or as a stand-alone executable in Windows or MacOS. The software, example data sets, and a user manual are available in the supplemental material to this paper and in public repositories including GitHub.

Conclusion

In this paper we develop an application of NMF to bivariate detrital data sets. We show that the algorithm can recover both the bivariate endmember distribution and also the mixing weights by factorizing mixtures of known sources. The recovered endmember distributions are almost identical to the known sources and the mixing weights show close correlation to the known mixing weights. We conclude that NMF provides a robust method of determining the endmember distributions and mixing weights in mixed two-dimensional detrital distributions.

After evaluating possible approaches to determining the optimum factorization rank, we conclude that breakpoint analysis provides the most robust method of determining the optimum rank. Bi-cross-validation yielded inaccurate and imprecise estimates of the factorization rank and number of sources. In contrast breakpoint analysis consistently yielded an optimum rank within one of the known number of sources.

Application of the method to 24 Proterozoic–Triassic samples from western Laurentia yielded an optimum rank of six. Factorization to six endmembers yielded distributions that closely match known potential sources on the northern, eastern, and southern margins of Laurentia. The mixing weight of these endmembers is broadly consistent with previous interpretations of Paleozoic–early Mesozoic sediment dispersal and suggests broad compatibility amongst previously published qualitative and quantitative interpretations of univariate detrital geochronology data, previously published qualitative interpretations of bivariate data, and the interpretations based on quantitative analysis of bivariate data presented here. Although broadly compatible, NMF of bivariate data sets revises some sediment transport reconstructions and clarifies early Paleozoic and Triassic sediment sources. Most notably, the revised provenance attributions support emergence of the Transcontinental Arch as a barrier to east–west transport in the late Cambrian and a Gondwanan source for Permo-Triassic zircons with evolved Hf isotopic compositions found in southern Laurentian strata.

Acknowledgements We are extremely grateful to Dr. E. Szymanski and an anonymous reviewer for helpful and detailed comments and to Dr. F. Cheng for editorial handling.

Author contributions **JES**: conceptualization (lead), data curation (equal), formal analysis (lead), methodology (equal), software (equal), writing – original draft (lead); **KES**: conceptualization (supporting), data curation (equal), formal analysis (equal), methodology (equal), software (equal), writing – original draft (supporting)

Funding This work was funded by the Unversity of British Columbia, the Natural Sciences and Engineering Research Council of Canada (Discovery Grant Program), and National Science Foundation (EAR-1824557).

Data availability All data generated or analysed during this study are included in this published article (and its supplementary information files).

Scientific editing by Feng Cheng

Correction notice: Equations 7 and 8 were incorrect and have been updated.

References

Ahmed, N., Natarajan, T. and Rao, K.R. 1974. Discrete cosine transform. *IEEE Transactions on Computers*, **100**, 90–93, https://doi.org/10.1109/T-C.1974.223784

Akaike, H. 1974. A new look at the statistical model identification. *IEEE Transactions on Automatic Control*, **19**, 716–723, https://doi.org/10.1109/TAC.1974.1100705

Andersen, T. 2014. The detrital zircon record: supercontinents, parallel evolution—Or coincidence? *Precambrian Research*, **244**, 279–287, https://doi.org/10.1016/j.precamres.2013.10.013

Andersen, T., Griffin, W.L. and Pearson, N.J. 2002. Crustal evolution in the SW Part of the Baltic Shield: the Hf isotope evidence. *Journal of Petrology*, **43**, 1725–1747, https://doi.org/10.1093/petrology/43.9.1725

Andersen, T., Griffin, W.L. and Sylvester, A.G. 2007. Sveconorwegian crustal underplating in southwestern Fennoscandia: LAM-ICPMS U–Pb and Lu–Hf isotope evidence from granites and gneisses in Telemark, southern Norway. *Lithos*, **93**, 273–287, https://doi.org/10.1016/j.lithos.2006.03.068

Andersen, T., Saeed, A., Gabrielsen, R.H. and Olaussen, S. 2011. Provenance characteristics of the Brumunddal sandstone in the Oslo Rift derived from U-Pb, Lu-Hf and trace element analyses of detrital zircons by laser ablation ICMPS. *Norwegian Journal of Geology/Norsk Geologisk Forening*, **91**.

Andresen, A., Agyei-Dwarko, N.Y., Kristoffersen, M. and Hanken, N.-M. 2014. A Timanian foreland basin setting for the late Neoproterozoic–Early Palaeozoic cover sequences (Dividal Group) of northeastern Baltica. *Geological Society, London, Special Publications*, **390**, 157–175, https://doi.org/10.1144/SP390.29

Anfinson, O.A., Leier, A.L., Gaschnig, R., Embry, A.F. and Dewing, K. 2012. U–Pb and Hf isotopic data from Franklinian Basin strata: insights into the nature of Crockerland and the timing of accretion, Canadian Arctic Islands. *Canadian Journal of Earth Sciences*, **49**, 1316–1328, https://doi.org/10.1139/e2012-067

Appleby, S.K., Gillespie, M.R., Graham, C.M., Hinton, R.W., Oliver, G.J. and Kelly, N.M. 2010. Do S-type granites commonly sample infracrustal sources?

New results from an integrated O, U–Pb and Hf isotope study of zircon. *Contributions to Mineralogy and Petrology*, **160**, 115–132, https://doi.org/10.1007/s00410-009-0469-3

Augland, L.E., Andresen, A., Corfu, F., Simonsen, S.L. and Andersen, T. 2012. The Beiarn Nappe Complex: a record of laurentian early silurian arc magmatism in the Uppermost Allochthon, Scandinavian Caledonides. *Lithos*, **146–147**, 233–252, https://doi.org/10.1016/j.lithos.2012.05.016

Barth, A.P., Wooden, J.L., Coleman, D.S. and Fanning, C.M. 2000. Geochronology of the Proterozoic basement of southwesternmost North America, and the origin and evolution of the Mojave crustal province. *Tectonics*, **19**, 616–629, https://doi.org/10.1029/1999TC001145

Belousova, E., Griffin, W., O'Reilly, S.Y. and Fisher, N. 2002. Igneous zircon: trace element composition as an indicator of source rock type. *Contributions to Mineralogy and Petrology*, **143**, 602–622, https://doi.org/10.1007/s00410-002-0364-7

Bickford, M., Mueller, P., Kamenov, G.D. and Hill, B.M. 2008. Crustal evolution of southern Laurentia during the Paleoproterozoic: insights from zircon Hf isotopic studies of ca. 1.75 Ga rocks in central Colorado. *Geology*, **36**, 555–558, https://doi.org/10.1130/G24700A.1

Bickford, M.E., McLelland, J.M., Mueller, P.A., Kamenov, G.D. and Neadle, M. 2010. Hafnium isotopic compositions of zircon from Adirondack AMCG suites: implications for the petrogenesis of anorthosites, gabbros, and granitic members of the suites. *The Canadian Mineralogist*, **48**, 751–761, https://doi.org/10.3749/canmin.48.2.751

Bleeker, W., Ketchum, J.W., Jackson, V.A. and Villeneuve, M.E. 1999. The central slave basement complex, part I: its structural topology and autochthonous cover. *Canadian Journal of Earth Sciences*, **36**, 1083–1109, https://doi.org/10.1139/e98-102

Brander, L., Söderlund, U.L.F. and Bingen, B. 2011. Tracing the 1271–1246 Ma Central Scandinavian Dolerite Group mafic magmatism in Fennoscandia: U–Pb baddeleyite and Hf isotope data on the Moslätt and Børgefjell dolerites. *Geological Magazine*, **148**, 632–643, https://doi.org/10.1017/S0016756811000033

Cecil, M.R., Gehrels, G., Ducea, M.N. and Patchett, P.J. 2011. U-Pb-Hf characterization of the central Coast Mountains batholith: implications for petrogenesis and crustal architecture. *Lithosphere*, **3**, 247–260, https://doi.org/10.1130/L134.1

Cecil, M.R., Ferrer, M.A., Riggs, N.R., Marsaglia, K., Kylander-Clark, A., Ducea, M.N. and Stone, P. 2019. Early arc development recorded in Permian–Triassic plutons of the northern Mojave Desert region, California, USA. *GSA Bulletin*, **131**, 749–765, https://doi.org/10.1130/B31963.1

Chamberlain, K.R., Frost, C.D. and Frost, B.R. 2003. Early Archean to Mesoproterozoic evolution of the Wyoming Province: Archean origins to modern lithospheric architecture. *Canadian Journal of Earth Sciences*, **40**, 1357–1374, https://doi.org/10.1139/e03-054

Chapman, A.D. and Laskowski, A.K. 2019. Detrital zircon U-Pb data reveal a Mississippian sediment dispersal network originating in the Appalachian orogen, traversing North America along its southern shelf, and reaching as far as the southwest United States. *Lithosphere*, **11**, 581–587, https://doi.org/10.1130/L1068.1

Cochrane, R. 2013. *U-Pb Thermochronology, Geochronology and Geochemistry of NW South America: Rift to Drift Transition, Active Margin Dynamics and Implications for the Volume Balance of Continents*. PhD thesis, University of Geneva.

Dickinson, W.R. and Gehrels, G.E. 2008. U-Pb ages of detrital zircons in relation to paleogeography: Triassic paleodrainage networks and sediment dispersal across southwest Laurentia. *Journal of Sedimentary Research*, **78**, 745–764, https://doi.org/10.2110/jsr.2008.088

Dickinson, W.R., Lawton, T.F. and Gehrels, G.E. 2009. Recycling detrital zircons: a case study from the Cretaceous Bisbee Group of southern Arizona. *Geology*, **37**, 503–506, https://doi.org/10.1130/G25646A.1

Doe, M.F., Jones III, J.V., Karlstrom, K.E., Dixon, B., Gehrels, G. and Pecha, M. 2013. Using detrital zircon ages and Hf isotopes to identify 1.48–1.45 Ga sedimentary basins and fingerprint sources of exotic 1.6–1.5 Ga grains in southwestern Laurentia. *Precambrian Research*, **231**, 409–421, https://doi.org/10.1016/j.precamres.2013.03.002

Domeier, M. and Torsvik, T.H., 2014. Plate tectonics in the late Paleozoic. *Geoscience Frontiers*, **5**, 303–350, https://doi.org/10.1016/j.gsf.2014.01.002

Draper, N.R. and Smith, H. 1998. *Applied Regresion Analysis*, 3rd edn. Wiley and Sons, New York.

Flowerdew, M., Chew, D., Daly, J. and Millar, I. 2009. Hidden Archaean and Palaeoproterozoic crust in NW Ireland? Evidence from zircon Hf isotopic data from granitoid intrusions. *Geological Magazine*, **146**, 903–916, https://doi.org/10.1017/S0016756809990227

Fonneland, H.C., Lien, T., Martinsen, O.J., Pedersen, R.B. and Košler, J. 2004. Detrital zircon ages: a key to understanding the deposition of deep marine sandstones in the Norwegian Sea. *Sedimentary Geology*, **164**, 147–159, https://doi.org/10.1016/j.sedgeo.2003.09.005

Fu, B., Page, F.Z. *et al.* 2008. Ti-in-zircon thermometry: applications and limitations. *Contributions to Mineralogy and Petrology* **156**, 197–215, https://doi.org/10.1007/s00410-008-0281-5

Fu, Y., Matsushima, S. and Yamanishi, K. 2019. Model selection for non-negative tensor factorization with minimum description length. *Entropy*, **21**, 632, https://doi.org/10.3390/e21070632

Fyffe, L.R., Barr, S.M. *et al.* 2009. Detrital zircon ages from Neoproterozoic and Early Paleozoic conglomerate and sandstone units of New Brunswick and coastal Maine: implications for the tectonic evolution of Ganderia.

Gehrels, G.E. and Dickinson, W.R. 2000. Detrital zircon geochronology of the Antler overlap and foreland basin assemblages, Nevada. *In*: Soreghan, M.J. and Gehrels, G.E. (eds) *Paleozoic and Triassic Paleogeography and Tectonics of Western Nevada and Northern California*. Geological Society of America, 57–63.

Gehrels, G. and Pecha, M. 2014. Detrital zircon U-Pb geochronology and Hf isotope geochemistry of Paleozoic and Triassic passive margin strata of western North America. *Geosphere*, **10**, 49–65, https://doi.org/10.1130/GES00889.1

Gehrels, G.E., Blakey, R., Karlstrom, K.E., Timmons, J.M., Dickinson, B. and Pecha, M. 2011. Detrital zircon U-Pb geochronology of Paleozoic strata in the Grand Canyon, Arizona. *Lithosphere*, **3**, 183–200, https://doi.org/10.1130/L121.1

Gifford, J.N., Malone, S.J. and Mueller, P.A. 2020. The Medicine Hat Block and the Early Paleoproterozoic Assembly of Western Laurentia. *Geosciences*, **10**, 271, https://doi.org/10.3390/geosciences10070271

Gleason, J.D., Gehrels, G.E., Dickinson, W.R., Patchett, P.J. and Kring, D.A. 2007. Laurentian sources for detrital zircon grains in turbidite and deltaic sandstones of the pennsylvanian haymond formation, marathon assemblage, West Texas, U.S.A. *J. Sedimentary Research*, **77**, 888–900, https://doi.org/10.2110/jsr.2007.084

Hartlaub, R., Heaman, L., Chacko, T. and Ashton, K. 2007. Circa 2.3-Ga magmatism of the Arrowsmith orogeny, Uranium City region, western Churchill craton, Canada. *The Journal of Geology*, **115**, 181–195, https://doi.org/10.1086/510641

Hawkins, D.P., Bowring, S.A., Ilg, B.R., Karlstrom, K.E. and Williams, M.L. 1996. U-Pb geochronologic constraints on the Paleoproterozoic crustal evolution of the Upper Granite Gorge, Grand Canyon, Arizona. *GSA Bulletin*, **108**, 1167–1181, https://doi.org/10.1130/0016-7606(1996)108<1167:UPGCOT>2.3.CO;2

Henderson, B.J., Collins, W.J., Murphy, J.B., Gutierrez-Alonso, G. and Hand, M. 2016. Gondwanan basement terranes of the Variscan–Appalachian orogen: Baltican, Saharan and West African hafnium isotopic fingerprints in Avalonia, Iberia and the Armorican Terranes. *Tectonophysics*, **681**, 278–304, https://doi.org/10.1016/j.tecto.2015.11.020

Hoffman, P.F. 1988. United plates of America, the birth of a craton: early Proterozoic assembly and growth of Laurentia. *Annual Review of Earth and Planetary Sciences*, **16**, 543–603, https://doi.org/10.1146/annurev.ea.16.050188.002551

Hoffman, P.F., Bally, A. and Palmer, A. 1989. Precambrian geology and tectonic history of North America. *In*: Bally, A. and Palmer, A. (eds), *The Geology of North America—an Overview*. The Geological Society of America, Boulder, 447–512.

Holland, M.E., Karlstrom, K. *et al.* 2015. An imbricate midcrustal suture zone: the Mojave-Yavapai province boundary in Grand Canyon, Arizona. *GSA Bulletin*, **127**, 1391–1410, https://doi.org/10.1130/B31232.1

Hoskin, P.W.O. and Schaltegger, U. 2003. The composition of zircon and igneous and metamorphic petrogenesis. *Reviews in Mineralogy and Geochemistry.*, **53**, 27–62, https://doi.org/10.2113/0530027

Ibañez-Mejia, M., Pullen, A., Pepper, M., Urbani, F., Ghoshal, G. and Ibañez-Mejia, J.C. 2018. Use and abuse of detrital zircon U-Pb geochronology—A case from the Río Orinoco delta, eastern Venezuela. *Geology*, **46**, 1019–22, https://doi.org/10.1130/G45596.1

Jackson, V.A., van Breemen, O. *et al.* 2013. U–Pb zircon ages and field relationships of Archean basement and Proterozoic intrusions, south-central Wopmay Orogen, NWT: implications for tectonic assignments. *Canadian Journal of Earth Sciences*, **50**, 979–1006, https://doi.org/10.1139/cjes-2013-0046

Kalsbeek, F., Nutman, A.P. and Taylor, P.N. 1993. Palaeoproterozoic basement province in the Caledonian fold belt of North-East Greenland. *Precambrian Research*, **63**, 163–178, https://doi.org/10.1016/0301-9268(93)90010-Y

Kalsbeek, F., Thrane, K., Higgins, A., Jepsen, H.F., Leslie, A.G., Nutman, A.P. and Frei, R. 2008. Polyorogenic history of the East Greenland Caledonides. *In*: Higgins, A.K., Gilotti, J.A. and Smith, M.P. (eds) *The Greenland Caledonides: Evolution of the Northeast Margin of Laurentia*. Geological Society of America Memoir, **202**, 55–72.

Karabinos, P., Macdonald, F.A. and Crowley, J.L. 2017. Bridging the gap between the foreland and hinterland I: Geochronology and plate tectonic geometry of Ordovician magmatism and terrane accretion on the Laurentian margin of New England. *American Journal of Science*, **317**, 515–554, https://doi.org/10.2475/05.2017.01

Key, R.M., Johnson, C.C. *et al.* 2012. Investigating high zircon concentrations in the fine fraction of stream sediments draining the Pan-African Dahomeyan Terrane in Nigeria. *Applied Geochemistry*, **27**, 1525–1539, https://doi.org/10.1016/j.apgeochem.2012.04.009

Kissock, J., Finzel, E., Malone, D. and Craddock, J. 2018. Lower–Middle Pennsylvanian strata in the North American midcontinent record the interplay between erosional unroofing of the Appalachians and eustatic sea-level rise. *Geosphere*, **14**, 141–161, https://doi.org/10.1130/GES01512.1

Kristoffersen, M., Andersen, T. and Andresen, A. 2014. U–Pb age and Lu–Hf signatures of detrital zircon from Palaeozoic sandstones in the Oslo Rift, Norway. *Geological Magazine*, **151**, 816–829, https://doi.org/10.1017/S0016756813000885

LaFlamme, C., Sylvester, P.J., Hinchey, A.M. and Davis, W.J. 2013. U–Pb age and Hf-isotope geochemistry of zircon from felsic volcanic rocks of the Paleoproterozoic Aillik Group, Makkovik Province, Labrador. *Precambrian Research*, **224**, 129–142, https://doi.org/10.1016/j.precamres.2012.09.005

Laskowski, A.K., DeCelles, P.G. and Gehrels, G.E. 2013. Detrital zircon geochronology of Cordilleran retroarc foreland basin strata, western North America. *Tectonics*, **32**, 1027–1048, https://doi.org/10.1002/tect.20065

Lawton, T.F. 1994. Tectonic setting of Mesozoic sedimentary basins, rocky Mountain region, United States. *In*: Caputo, M.V., Peterson, J.A., Franczyk, K.J. (eds) *Mesozoic Systems of the Rocky Mountain Region, USA*. Rocky Mountain Section (SEPM), 1–26.

Lawton, T.F., Buller, C.D. and Parr, T.R. 2015. Provenance of a Permian erg on the western margin of Pangea: depositional system of the Kungurian (late Leonardian) Castle Valley and White Rim sandstones and subjacent Cutler Group, Paradox Basin, Utah, USA. *Geosphere*, **11**, 1475–1506, https://doi.org/10.1130/GES01174.1

Leary, R.J., Umhoefer, P., Smith, M.E. and Riggs, N. 2017. A three-sided orogen: A new tectonic model for Ancestral Rocky Mountain uplift and basin development. *Geology*, **45**, 735–738, https://doi.org/10.1130/G38830.1

Leary, R.J., Umhoefer, P. *et al.* 2020. Provenance of Pennsylvanian-Permian sedimentary rocks associated with the Ancestral Rocky Mountains orogeny in southwestern Laurentia: implications for continental-scale Laurentian sediment transport systems. *Lithosphere*, **12**, **88**–121, https://doi.org/10.1130/L1115.1

Linde, G.M., Trexler, J.H., Cashman, P.H., Gehrels, G. and Dickinson, W.R. 2016. Detrital zircon U-Pb geochronology and Hf isotope geochemistry of the Roberts Mountains allochthon: new insights into the early Paleozoic tectonics of western North America. *Geosphere*, **12**, 1016–1031, https://doi.org/10.1130/GES01252.1

Linde, G.M., Trexler, J.H.Jr., Cashman, P.H., Gehrels, G. and Dickinson, W.R. 2017. Three-dimensional evolution of the early paleozoic western laurentian margin: new insights from detrital Zircon U-Pb Geochronology and Hf isotope geochemistry of the harmony formation of Nevada. *Tectonics*, **36**, 2347–2369, https://doi.org/10.1002/2017TC004520

Liu, L. and Stockli, D.F. 2019. U-Pb ages of detrital zircons in lower Permian sandstone and siltstone of the Permian Basin, west Texas, USA: evidence of dominant Gondwanan and peri-Gondwanan sediment input to Laurentia. *GSA Bulletin*, **132**, 245–262, https://doi.org/10.1130/B35119.1

Macdonald, F.A., Ryan-Davis, J., Coish, R.A., Crowley, J.L. and Karabinos, P. 2014. A newly identified Gondwanan terrane in the northern Appalachian Mountains: implications for the Taconic orogeny and closure of the Iapetus Ocean. *Geology*, **42**, 539–542, https://doi.org/10.1130/G35659.1

Malkowski, M.A., Sharman, G.R., Johnstone, S.A., Grove, M.J., Kimbrough, D.L. and Graham, S.A. 2019. Dilution and propagation of provenance trends in sand and mud: geochemistry and detrital zircon geochronology of modern sediment from central California (USA). *American Journal of Science*, **319**, 846–902, https://doi.org/10.2475/10.2019.02

Malone, S.J. 2012. *Tectonic Evolution of Northern Ellesmere Island: Insights From the Pearya Terrane, Ellesmerian Clastic Wedge and Sverdrup Basin*. University of Iowa.

Malusà, M.G., Carter, A., Limoncelli, M., Villa, I.M. and Garzanti, E. 2013. Bias in detrital zircon geochronology and thermochronometry. *Chemical Geology*, **359**, 90–107, https://doi.org/10.1016/j.chemgeo.2013.09.016

Malusà, M.G., Resentini, A. and Garzanti, E. 2016. Hydraulic sorting and mineral fertility bias in detrital geochronology. *Gondwana Research*, **31**, 1–19, https://doi.org/10.1016/j.gr.2015.09.002

Martens, U., Weber, B. and Valencia, V.A. 2010. U/Pb geochronology of Devonian and older Paleozoic beds in the southeastern Maya block, Central America: its affinity with peri-Gondwanan terranes. *GSA Bulletin*, **122**, 815–829, https://doi.org/10.1130/B26405.1

May, S.R., Gray, G.G., Summa, L.L., Stewart, N.R., Gehrels, G.E. and Pecha, M.E. 2013. Detrital zircon geochronology from the Bighorn Basin, Wyoming, USA: implications for tectonostratigraphic evolution and paleogeography. *GSA Bulletin*, **125**, 1403–1422, https://doi.org/10.1130/B30824.1

McClelland, W.C., Gilotti, J.A., Ramarao, T., Stemmerik, L. and Dalhoff, F., 2016. Carboniferous basin in Holm Land records local exhumation of the North-East Greenland Caledonides: implications for the detrital zircon signature of a collisional orogen. *Geosphere*, **12**, 925–947, https://doi.org/10.1130/GES01284.1

McKerrow, W., Mac Niocaill, C. and Dewey, J. 2000. The Caledonian orogeny redefined. *Journal of the Geological Society, London,*, **157**, 1149–1154, https://doi.org/10.1144/jgs.157.6.1149

McMillan, N. and McLemore, V. 2004. Cambrian-Ordovician magmatism and extension in New Mexico and Colorado. *New Mexico Bureau of Geology & Mineral Resources Bulletin*, **160**, 1–11.

Midwinter, D., Hadlari, T., Davis, W.J., Dewing, K. and Arnott, R.W.C. 2016. Dual provenance signatures of the Triassic northern Laurentian margin from detrital-zircon U-Pb and Hf-isotope analysis of Triassic–Jurassic strata in the Sverdrup Basin. *Lithosphere*, **8**, 668–683, https://doi.org/10.1130/L517.1

Moecher, D.P. and Samson, S.D. 2006. Differential zircon fertility of source terranes and natural bias in the detrital zircon record: implications for sedimentary provenance analysis. *Earth and Planetary Science Letters*, **247**, 252–266, https://doi.org/10.1016/j.epsl.2006.04.035

Mueller, P.A., Kamenov, G.D., Heatherington, A.L. and Richards, J. 2008. Crustal evolution in the southern Appalachian orogen: evidence from Hf isotopes in detrital zircons. *The Journal of Geology*, **116**, 414–422, https://doi.org/10.1086/589311

Müller, R.D., Cannon, J. *et al.* 2018. GPlates: building a virtual Earth through deep time. *Geochemistry Geophysics Geosystems*, **19**, 2243–2261, https://doi.org/10.1029/2018GC007584

Mumford, T. 2013. *Petrology of the Blatchford Lake Instrusive Suite, Northwest Territories, Canada*. Carleton University.

Nutman, A.P., Kalsbeek, F. and Friend, C.R., 2008. The Nagssugtoqidian orogen in South-East Greenland: evidence for Paleoproterozoic collision and plate assembly. *American Journal of Science*, **308**, 529–572, https://doi.org/10.2475/04.2008.06

Ootes, L., Buse, S., Davis, W. and Cousens, B. 2005. *U-Pb Ages From the Northern Wecho River Area, Southwestern Slave Province, Northwest Territories: Constraints on Late Archean Plutonism and Metamorphism*. Natural Resources Canada, Geological Survey of Canada.

Owen, A.B. and Perry, P.O. 2009. Bi-cross-validation of the SVD and the nonnegative matrix factorization. *The Annals of Applied Statistics*, **3**, 564–594, https://doi.org/10.1214/08-AOAS227

Partin, C.A., Bekker, A., Sylvester, P.J., Wodicka, N., Stern, R.A., Chacko, T. and Heaman, L.M. 2014. Filling in the juvenile magmatic gap: evidence for uninterrupted Paleoproterozoic plate tectonics. *Earth and Planetary Science Letters*, **388**, 123–133, https://doi.org/10.1016/j.epsl.2013.11.041

Peacock, J.A. 1983. Two-dimensional goodness-of-fit testing in astronomy. *Monthly Notices of the Royal Astronomical Society*, **202**, 615–627, https://doi.org/10.1093/mnras/202.3.615

Percival, J.A., Bleeker, W., Cook, F.A., Rivers, T., Ross, G. and van Staal, C. 2004. PanLITHOPROBE Workshop IV: intra-orogen correlations and comparative orogenic anatomy. *Geoscience Canada*, **31**.

Pettit, B.S., Blum, M., Pecha, M., McLean, N., Bartschi, N.C. and Saylor, J.E. 2019. Detrital-Zircon U-Pb Paleodrainage Reconstruction and Geochronology of the Campanian Blackhawk–Castlegate Succession, Wasatch Plateau and Book Cliffs, Utah, U.S.A. *Journal of Sedimentary Research*, **89**, 273–292, https://doi.org/10.2110/jsr.2019.18

Pollock, J.C., Sylvester, P.J. and Barr, S.M. 2015. Lu–Hf zircon and Sm–Nd whole-rock isotope constraints on the extent of juvenile arc crust in Avalonia: examples from Newfoundland and Nova Scotia, Canada. *Canadian Journal of Earth Sciences*, **52**, 161–181, https://doi.org/10.1139/cjes-2014-0157

Press, W.H. and Teukolsky, S.A. 1988. Kolmogorov-Smirnov test for two-dimensional data: how to tell whether a set of (x, y) data paints are consistent with a particular probability distribution, or with another data set. *Computers in Physics*, **2**, 74–77, https://doi.org/10.1063/1.4822753

Puetz, S.J. and Condie, K.C. 2019. Time series analysis of mantle cycles Part I: periodicities and correlations among seven global isotopic databases. *Geoscience Frontiers*, **10**, 1305–1326, https://doi.org/10.1016/j.gsf.2019.04.002

Rahl, R.M., Reiners, P.W., Campbell, I.H., Nicolescu, S. and Allen, C.M. 2003. Combined single-grain (U-Th)/He and U/Pb dating of detrital zircons from the Navajo Sandstone, Utah. *Geology*, **31**, 761–764, https://doi.org/10.1130/G19653.1

Raj, B., Virtanen, T., Chaudhuri, S. and Singh, R. 2010. Non-negative matrix factorization based compensation of music for automatic speech recognition. Eleventh Annual Conference of the International Speech Communication Association, Chiba, Japan.

Rajabi, R. and Ghassemian, H. 2014. Spectral unmixing of hyperspectral imagery using multilayer NMF. *IEEE Geoscience and Remote Sensing Letters*, **12**, 38–42, https://doi.org/10.1109/LGRS.2014.2325874

Rehnström, E.F. 2010. Prolonged Paleozoic magmatism in the East Greenland Caledonides: some constraints from U-Pb ages and Hf isotopes. *The Journal of Geology*, **118**, 447–465, https://doi.org/10.1086/655010

Riggs, N.R., Oberling, Z.A., Howell, E.R., Parker, W.G., Barth, A.P., Cecil, M.R. and Martz, J.W. 2016. Sources of volcanic detritus in the basal Chinle Formation, southwestern Laurentia, and implications for the Early Mesozoic magmatic arc. *Geosphere*, **12**, 439–463, https://doi.org/10.1130/GES01238.1

Roberts, N.M. and Spencer, C.J. 2015. The zircon archive of continent formation through time. *Geological Society, London, Special Publications*, **389**, 197–225, https://doi.org/10.1144/SP389.14

Røhr, T.S., Andersen, T. and Dypvik, H. 2008. Provenance of Lower Cretaceous sediments in the Wandel Sea Basin, North Greenland. *Journal of the Geological Society, London*, **165**, 755–767, https://doi.org/10.1144/0016-76492007-102

Røhr, T.S., Andersen, T., Dypvik, H. and Embry, A.F. 2010. Detrital zircon characteristics of the Lower Cretaceous Isachsen Formation, Sverdrup Basin: source constraints from age and Hf isotope data. *Canadia Journal of Earth Sciences*, **47**, 255–271, https://doi.org/10.1139/E10-006

Ross, G.M. 2002. Evolution of Precambrian continental lithosphere in Western Canada: results from Lithoprobe studies in Alberta and beyond. *Canadian Journal of Earth Sciences*, **39**, 413–437, https://doi.org/10.1139/e02-012

Ross, G., Parrish, R., Villeneuve, M. and Bowring, S. 1991. Geophysics and geochronology of the crystalline basement of the Alberta Basin, western Canada. *Canadian Journal of Earth Sciences*, **28**, 512–522, https://doi.org/10.1139/e91-045

Saylor, J.E. and Sundell, K.E. 2016. Quantifying comparison of large detrital geochronology data sets. *Geosphere*, **12**, 203–220, https://doi.org/10.1130/GES01237.1

Saylor, J.E., Stockli, D.F., Horton, B.K., Nie, J. and Mora, A., 2012. Discriminating rapid exhumation from syndepositional volcanism using detrital zircon double dating: implications for the tectonic history of the Eastern Cordillera, Colombia. *GSA Bulletin*, **124**, 762–779, https://doi.org/10.1130/B30534.1

Saylor, J.E., Knowles, J.N., Horton, B.K., Nie, J.S. and Mora, A. 2013. Mixing of source populations recorded in detrital Zircon U-Pb age spectra of modern river sands. *Journal of Geology*, **121**, 17–33, https://doi.org/10.1086/668683

Saylor, J.E., Jordan, J.C., Sundell, K.E., Wang, X., Wang, S. and Deng, T., 2017. Topographic growth of the Jishi Shan and its impact on basin and hydrology evolution, NE Tibetan Plateau. *Basin Research*, **30**, 544–563, https://doi.org/10.1111/bre.12264

Saylor, J.E., Sundell, K.E. and Sharman, G.R. 2019. Characterizing sediment sources by non-negative matrix factorization of detrital geochronological data. *Earth and Planetary Science Letters*, **512**, 46–58, https://doi.org/10.1016/j.epsl.2019.01.044

Schwarz, G. 1978. Estimating the dimension of a model. *The Annals of Statistics*, **6**, 461–464, https://doi.org/10.1214/aos/1176344136

Scotese, C.R. 2016. PALEOMAP PaleoAtlas for GPlates, PALEOMAP Project.

Sharman, G.R. and Johnstone, S.A. 2017. Sediment unmixing using detrital geochronology. *Earth and Planetary Science Letters.*, **477**, 183–194, https://doi.org/10.1016/j.epsl.2017.07.044

Shiels, C., Partin, C.A. and Stern, R.A. 2017. An integrated U-Pb, Hf, and O isotopic provenance analysis of the Paleoproterozoic Murmac Bay Group, northern Saskatchewan, Canada. *Precambrian Research*, **302**, 18–32, https://doi.org/10.1016/j.precamres.2017.09.015

Sláma, J. and Košler, J. 2012. Effects of sampling and mineral separation on accuracy of detrital zircon studies. *Geochemistry Geophysics Geosystems.*, **13**, https://doi.org/10.1029/2012GC004106

Slama, J., Walderhaug, O., Fonneland, H., Kosler, J. and Pedersen, R.B. 2011. Provenance of Neoproterozoic to upper Cretaceous sedimentary rocks, eastern Greenland: implications for recognizing the sources of sediments in the Norwegian Sea. *SedimentaryGeology*, **238**, 254–267, https://doi.org/10.1016/j.sedgeo.2011.04.018

Smith, T.M., Lapen, T.J., Sundell, K.E., Hatfield, K., Saylor, J.E. and Leary, R.J. 2019. Central Colorado Trough sediment source isolation: Petrochronologic source discrimination applied to an Ancestral Rocky Mountain basin. GSA Annual Meeting, Phoenix, AZ.

Smith, T.M., Sundell, K.E. *et al.* 2020. Drainage reorganization and Laramide tectonics in north-central New Mexico and downstream effects in the Gulf of Mexico. *Basin Research*, **32**, 419–452, https://doi.org/10.1111/bre.12373.

Spencer, C.J., Dyck, B., Mottram, C.M., Roberts, N.M., Yao, W.-H. and Martin, E.L. 2019. Deconvolving the pre-Himalayan Indian margin–tales of crustal growth and destruction. *Geoscience Frontiers*, **10**, 863–872, https://doi.org/10.1016/j.gsf.2018.02.007

Squires, S., Prügel-Bennett, A. and Niranjan, M. 2017. Rank selection in nonnegative matrix factorization using minimum description length. *Neural Computation*, **29**, 2164–2176, https://doi.org/10.1162/neco_a_00980

Stewart, E.D., Link, P.K., Fanning, C.M., Frost, C.D. and McCurry, M. 2010. Paleogeographic implications of non–North American sediment in the Mesoproterozoic upper Belt Supergroup and Lemhi Group, Idaho and Montana, USA. *Geology*, **38**, 927–930, https://doi.org/10.1130/G31194.1

Sundell, K.E. and Saylor, J.E. 2017. Unmixing detrital geochronology age distributions. *Geochemistry*, *Geophysics, Geosystems*,**18**, 2872–2886, https://doi.org/10.1002/2016GC006774

Sundell, K.E. and Saylor, J.E. 2021. Two-dimensional quantitative comparison of density distributions in detrital geochronology and geochemistry. *Geochemistry, Geophysics, Geosystems*, e2020GC009559, https://doi.org/10.1029/2020GC00955

Sundell, K., Saylor, J.E. and Pecha, M. 2019. Provenance and recycling of detrital zircons from Cenozoic Altiplano strata and the crustal evolution of western South America from combined U-Pb and Lu-Hf isotopic analysis. *In*: Horton, B.K. and Folguera, A. (eds) *Andean Tectonics*. Elsevier, 363–397.

Thériault, R.J. and Ross, G.M. 1991. Nd isotopic evidence for crustal recycling in the ca. 2.0 Ga subsurface of western Canada. *Canadian Journal of Earth Sciences*, **28**, 1140–1147, https://doi.org/10.1139/e91-104

Thomas, W.A. 2011. Detrital-zircon geochronology and sedimentary provenance. *Lithosphere*, **3**, 304–308, https://doi.org/10.1130/RF.L001.1

Thomas, W.A. 2014. A mechanism for tectonic inheritance at transform faults of the Iapetan margin of Laurentia. *Geoscience Canada*, **41**, 321–344, https://doi.org/10.12789/geocanj.2014.41.048

Thomas, W.A., Gehrels, G.E. and Romero, M.C. 2016. Detrital zircons from crystalline rocks along the Southern Oklahoma fault system, Wichita and Arbuckle Mountains, USA. *Geosphere*, **12**, 1224-1234, https://doi.org/10.1130/GES01316.1

Thomas, W.A., Gehrels, G.E., Greb, S.F., Nadon, G.C., Satkoski, A.M. and Romero, M.C. 2017. Detrital zircons and sediment dispersal in the Appalachian foreland. *Geosphere*, **13**, 2206–2230, https://doi.org/10.1130/GES01525.1

Thomas, W.A., Gehrels, G.E. *et al.* 2020. Detrital zircons and sediment dispersal in the eastern Midcontinent of North America. *Geosphere*, **16**, 817–843, https://doi.org/10.1130/GES02152.1

van Staal, C.R., Whalen, J.B., Valverde-Vaquero, P., Zagorevski, A. and Rogers, N. 2009. Pre-Carboniferous, episodic accretion-related, orogenesis along the Laurentian margin of the northern Appalachians. *Geological Society, London, Special Publications*, **327**, 271–316, https://doi.org/10.1144/SP327.13

Vermeesch, P. 2013. Multi-sample comparison of detrital age distributions. *Chemical Geology*, **341**, 140–146, https://doi.org/10.1016/j.chemgeo.2013.01.010

Villeneuve, M., Ross, G., Theriault, R., Miles, W., Parrish, R. and Broome, J. 1993. *Tectonic Subdivision and U-Pb Geochronology of the Crystalline Basement of the Alberta Basin, Western Canada*. Geological Survey of Canada.

Waite, L., Fan, M., Collins, D., Gehrels, G. and Stern, R.J. 2020. Detrital zircon provenance evidence for an early Permian longitudinal river flowing into the Midland Basin of west Texas. *International Geology Review*, **62**, 1224–1244, https://doi.org/10.1080/00206814.2020.1756930

Weber, B., Scherer, E.E., Schulze, C., Valencia, V.A., Montecinos, P., Mezger, K. and Ruiz, J. 2010. U–Pb and Lu–Hf isotope systematics of lower crust from central-southern Mexico–Geodynamic significance of Oaxaquia in a Rodinia Realm. *Precambrian Research*, **182**, 149–162, https://doi.org/10.1016/j.precamres.2010.07.007

Willner, A., Barr, S., Gerdes, A., Massonne, H.-J. and White, C. 2013. Origin and evolution of Avalonia: evidence from U–Pb and Lu–Hf isotopes in zircon from the Mira terrane, Canada, and the Stavelot–Venn Massif, Belgium. *Journal of the Geological Society, London*, **170**, 769–784, https://doi.org/10.1144/jgs2012-152

Wooden, J., Stacey, J., Howard, K.A., Doe, B. and Miller, D. 1988. Pb isotopic evidence for the formation of Proterozoic crust in the southwestern United States.

Wooden, J.L., Barth, A.P. and Mueller, P.A. 2013. Crustal growth and tectonic evolution of the Mojave crustal province: Insights from hafnium isotope systematics in zircons. *Lithosphere*, **5**, 17–28, https://doi.org/10.1130/L218.1

Zirakparvar, N.A., Setera, J., Mathez, E., Vantongeren, J. and Fossum, R. 2017. The pre-Atlantic Hf isotope evolution of the east Laurentian continental margin: insights from zircon in basement rocks and glacial tillites from northern New Jersey and southeastern New York. *Lithos*, **272**, 69–83, https://doi.org/10.1016/j.lithos.2016.11.023